D-β-hydroxybutyrate stabilizes hippocampal CA3-CA1 circuit during acute insulin resistance.

Bartosz Kula[1], Botond Antal[2,3], Corey Weistuch[4], Florian Gackière[5], Alexander Barre[5], Victor Velado[6], Jeffrey M Hubbard[5], Maria Kukley[7,8], Lilianne R Mujica-Parodi[2,3,9,*], and Nathan A Smith[1,6,10,*].

1 Del Monte Institute for Neuroscience, Department of Neuroscience, University of Rochester, School of Medicine and Dentistry, Rochester, USA

2 Department of Biomedical Engineering, Stony Brook University, Stony Brook, USA

3 Athinoula A. Martinos Center for Biomedical Imaging, Massachusetts General Hospital and Harvard Medical School, Boston, USA

4 Department of Medical Physics, Memorial Sloan Kettering Cancer Center, New York, NY, USA

5 Neuroservices Alliance, Les Jardins de l'Entreprise, Quartier de le Confrérie, Le Puy Ste Réparade, France

6 Center for Neuroscience Research, Children's National Research Institute, Children's National Hospital, Washington D.C., USA

7 Achucarro Basque Center for Neuroscience, Leioa, Spain

8 Ikerbasque - Basque Foundation for Science, Bilbao, Spain

9 Laufer Center for Physical and Quantitative Biology, Stony Brook University, Stony Brook, USA

10 George Washington University School of Medicine and Health Sciences, Washington D.C., USA

* Corresponding authors: lilianne.strey@stonybrook.edu (LMP);
Nathan_Smith@urmc.rochester.edu (NAS)

1. **Abstract**

The brain primarily relies on glycolysis for mitochondrial respiration but switches to alternative fuels such as ketone bodies (KBs) when less glucose is available. Neuronal KB uptake, which does not rely on glucose transporter 4 (GLUT4) or insulin, has shown promising clinical applicability in alleviating the neurological and cognitive effects of disorders with hypometabolic components. However, the specific mechanisms by which such interventions affect neuronal functions are poorly understood. In this study, we pharmacologically blocked GLUT4 to investigate the effects of exogenous KB D-β-hydroxybutyrate (D-βHb) on mouse brain metabolism during acute insulin resistance (AIR). We found that both AIR and D-βHb had distinct impacts across neuronal compartments: AIR decreased synaptic activity and long-term potentiation (LTP) and impaired axonal conduction, synchronization, and action potential (AP) properties, while D-βHb rescued neuronal functions associated with axonal conduction, synchronization and LTP.

Keywords: beta-hydroxybutyrate, GLUT4, hippocampus, insulin resistance, ketone bodies

2. **Significance statement**

This study investigates the impact of acute insulin resistance on the functionality of the hippocampal circuit and the potential protective effects of ketone body supplementation. By inhibiting GLUT4 receptors to induce acute insulin resistance, we reveal several detrimental changes caused by impaired neuronal glucose uptake. These changes include impairments in synaptic activity, axonal conduction, and neuronal firing properties. The study further examines the distinctive effects of acute insulin resistance (AIR) and the rescue agent D-βHb on synaptic activity, long-term potentiation, axonal conduction, synchronization, and neuronal firing. By shedding light on neuronal responses during insulin resistance, this investigation advances our understanding of neurological disorders associated with hypometabolism and highlights the potential therapeutic value of D-βHb.

3. **Introduction**

Over the past two decades, research on insulin signaling in the brain has become increasingly important in studies of type 2 diabetes mellitus (T2DM) and Alzheimer's disease (AD) [1,2]. Insulin plays a critical role in memory formation processes in the hippocampus, and systemic insulin resistance can interfere with hippocampal metabolism and cognitive function, as shown by various studies [3,4]. Additionally, insulin is an essential element in memory processing in the hippocampus and a vital mediator of cognitive impairment in patients with T2DM and AD due to its function in promoting GLUT4 translocation [5,6]. Although insulin from the blood crosses the

blood–brain barrier, research suggests supplementary local insulin synthesis and release in the brain [7], which enhances the pro-cognitive effects of brain glucose [8]. Therefore, impaired glucose uptake in the hippocampus may contribute to cognitive decline associated with aging, T2DM, and AD [9,10,11].

This relationship has led to the hypothesis that brain hypometabolism reflects encroaching neuronal insulin resistance. The hippocampus is highly enriched with GLUT4 receptors, which are the primary neuronal insulin-dependent glucose transporter, particularly in brain areas with high concentrations of insulin receptors and relatively high neuronal activity [8,12,13]. Insulin acts by enhancing GLUT4 translocation across neuronal membranes under the regulation of phosphatidylinositol 3-kinase (PI3K), which promotes memory formation [14,15]. During memory formation, GLUT4 is primarily expressed in the soma rather than in the more metabolically active hippocampal neuropil [16,17], suggesting that the primary effect of insulin may be the maintenance of neuronal firing. Mouse models of AD or diet-induced obesity (DIO) showed blunting of the pro-cognitive effects of intrahippocampal insulin injections and decreased local glucose metabolism [18,19], coupled with neuronal hyperexcitability with epileptiform spikes and impairment of GLUT4 translocation [20].

During periods with lower glucose availability, ketone bodies (KBs) supplement metabolism as an alternative fuel source [21,22]. The ketogenic diet has shown pro-cognitive benefits in patients suffering from T2DM or AD. These benefits of the ketogenic diet may arise due to reduced neuronal firing rates during ketosis [23,24], increased ATP:ADP ratios [25], increased secretion of GABA due to substantial formation of acetyl-CoA [26], equilibration of the NAD:NADH ratio, and reduced production of free radicals, which together may help to temper neuronal hyperexcitability and its metabolic consequences [27,28].

In addition, KBs are crucial in protecting mitochondria from acute metabolic stress by preventing mitochondrial permeability transition (mPT) through their effects on intracellular calcium levels [29,30]. Furthermore, KBs can affect neuronal firing by promoting the opening of ATP-sensitive K^+ channels (K-ATP), thus reducing the cytosolic pool of ATP generated from glycolysis [24,30].

Exogenous KBs, such as *D*-β-hydroxy-butyrate (D-βHb) ester, can increase KB levels in circulation without the severe dietary restrictions of the ketogenic diet [31,32]. Whether exogenous KBs maintain their neuroprotective effects in patients with normal plasma glucose levels remains unclear; however, recent studies have shown that in healthy adults, D-βHb led to increased overall brain activity and stabilized functional networks [33,34].

These observations led us to hypothesize that exogenous KBs could be utilized to rescue neuronal metabolism after cerebral insulin resistance. To test this hypothesis, we established a murine hippocampal model of acute insulin resistance (AIR) through the inhibition of GLUT4 by administration of indinavir [35,36]. We then studied how neuron-specific insulin resistance affected hippocampal neurons in the CA3-CA1 circuit, a model circuit for studying learning and

memory. We tested the effects of D-βHb during AIR to determine the therapeutic potential of exogenous KBs in hypoglycemic animals. To evaluate the circuit-wide effects on synaptic and axonal function, we obtained field potential recordings in the hippocampi of the treated mice and patch-clamp recordings in hippocampal slices to assess the in vitro effects of AIR and D-βHb on the electrophysiological properties of CA1 pyramidal neurons and CA1 fast-spiking interneurons (FSIs). Finally, we used computational modeling approaches to relate our electrophysiological results and Na^+/K^+ ATPase dysfunction as the potential reason for the detrimental changes observed during AIR.

4. **Results**

Various paradigms of synaptic plasticity associated with learning and memory have been identified in the hippocampus. Many studies have investigated long-term potentiation (LTP), long-term depression (LTD), spike-timing-dependent plasticity, and excitatory postsynaptic potential (EPSP)-spike potentiation in hippocampal circuits, making the hippocampus a classic system for studying neuroplasticity. Furthermore, the simple cytoarchitecture of the hippocampus makes it an ideal model system. In this study, we utilized indinavir, a potent GLUT4 receptor blocker, to pharmacologically induce AIR in hippocampal slices. Our investigation focused on the stratum radiatum of CA1, where numerous synapses are formed between Schaffer collaterals (SCOs) and the apical dendrites of pyramidal neurons.

4.1 Synaptic activity and LTP, but not fiber volleys (FVs), are adversely affected by AIR and are not reversed by either 0.1 mM or 1 mM D-βHb.

To test synaptic transmission within CA1 for a wide range of energetic demands, we measured the circuit's response under 3 different stimulation paradigms. First, we applied mild physiological stimulation (not imposing high energetic demands [37,38]), consisting of paired stimulation applied at 25 Hz, repeated every 20 s over 30-60 trials [**Fig. 1A-F**].

During the AIR condition, we observed strong decreases in field excitatory postsynaptic potential (fEPSP) amplitudes, -39.23 ± 8.72% (1st stimulation) and -38.79 ± 8.93% (2nd stimulation), compared to baseline [**Fig. 1A**]. The amplitude did not recover when D-βHb was applied at low (0.1 mM) [+13.10 ± 6.64% and +14.07 ± 6.76%, **Fig. 1A**, p=0.34, p=0.30] or high (1 mM) concentrations [**Fig. 1A**, -5.98 ± 6.13% and -5.81 ± 6.26%, p=0.88; p=0.56]. No changes in the paired-pulse ratio (PPR) were observed in any of the conditions [**Fig. 1B**, Control: 1.89; AIR: 1.92; 0.1 mM D-βHb+AIR: 2.00; 1 mM D-βHb+AIR: 1.88; p=0.54], suggesting that the activity at the synaptic sites remained largely unchanged.

When applied over sufficient time, our paired stimulation triggered LTP in CA1, as evidenced by a gradual increase in the fEPSP amplitude [**Fig. 1C, top**] but no change in the PPR [**Fig. 1C, bottom**]. Therefore, we compared the LTP magnitude between the groups by calculating the ratio of the EPSP amplitudes during the first 10 min and the amplitudes at 40 ± 10 min [**Fig. 1D-F**]. The control condition showed the strongest LTP ratio of 1.53 ± 0.13. LTP induction was almost abolished during AIR [**Fig. 1E**, 1.06 ± 0.06 ratio; -30.66 ± 9.42% reduction vs. control, p=0.018], and 0.1 mM D-βHb did not reverse this effect [**Fig. 1E**, 1.08 ± 0.08, +1.25 ± 6.61% AIR vs. D-βHb+AIR 0.1 mM, p > 0.99]; however, 1 mM D-βHb did reverse this effect [**Fig. 1E**, 1.39 ± 0.10, +21.19 ± 7.64% AIR vs. D-βHb+AIR 1 mM, p=0.044].

Moreover, we found no significant effects of either AIR or D-βHb+AIR on the amplitudes of the fiber volleys (FVs) [**Fig. 1F**, Control: 1.03 ± 0.08 mV; AIR: 0.89 ± 0.07; D-βHb+AIR 0.1 mM: 0.85 ± 0.08; D-βHb+AIR 1 mM: 1.03 ± 0.12; p=0.40]. Next, we tested whether the circuit would behave differently under a stronger stimulation that imposed greater metabolic demands. We stimulated the Schaffer collaterals with 20 pulses applied at 25 Hz, with 20 s breaks between trials. To ensure that the onset of LTP did not skew the results, we recorded all train stimulations at least 40 min after the paired stimulation paradigm.

All compared groups showed potentiation of fEPSP amplitudes during the train, reaching a peak at stimuli 5-6. Thereafter, the amplitudes decreased slightly but remained potentiated [**Fig. S1A, B**]. Interestingly, throughout the entire stimulation period, the fEPSP amplitudes matched the differences we observed during the paired stimulation experiments [**Fig. S1B**; at stimulus 5: -34.25 ± 11.80% Control vs. AIR, p=0.031; -40.54 ± 11.48% Control vs. 1 mM D-βHb+AIR, p=0.000044; +3.37 ± 7.80 AIR vs. 0.1 mM D-βHb+AIR, p = 0.99; -25.21 ± 7.36% AIR vs. 1 mM D-βHb+AIR, p=0.0054]. The FV amplitudes followed a different pattern, with potentiation at stimulus 2, followed by a consistent decline to approximately 70% of the initial amplitude [**Fig. S1C**]. Similar to the paired stimulation experiments, no statistically significant differences were observed between groups at any time point during the train stimulations [**Fig. S1C**; p=0.16 to 0.40].

Finally, we examined the hippocampal circuit under intense nonphysiological stimulation conditions. This involved applying long trains of 50 stimuli at 25 Hz, spanning across 60 trials with a 20 s break between each trial. The responses during this specific stimulation condition varied among trials, making it inappropriate to average the values over the entire stimulation period. As a result, we represent the fEPSP and FV amplitudes as heatmaps. In these heatmaps, each point represents the group's mean response to a single stimulus at a given time point.

Consistent with our previous results, we observed a period of fEPSP amplitude potentiation followed by a steady decline [**Fig. S2A-D**; at maximum, trial 4-6, stimuli 7-9: -34.81 ± 10.56% Control vs. AIR, p=0.0084; -48.27 ± 11.37% Control vs. 1 mM D-βHb+AIR, p=0.00065; +10.19 ± 11.39% AIR vs. 0.1 mM D-βHb+AIR, p=0.59; -13.66 ± 9.08% AIR vs. 1 mM D-βHb+AIR]. Synaptic

170 depression was first observed during the final stimuli of the stimulation trains, approximately 3
171 min into the stimulation period, and became more prominent with each subsequent train
172 stimulation application [**Fig. S2A-D**]. In general, the fEPSP amplitudes in the control and AIR
173 groups differed substantially during the first 7 min of the recordings [**Fig. S2A**]. The fEPSP
174 amplitudes in the control and 1 mM D-βHb+AIR groups also differed throughout most of the
175 stimulation trains [**Fig. S2B**], but the fEPSP amplitudes in the 0.1 mM D-βHb+AIR and AIR groups
176 scarcely differed except at the end of the stimulation trains [**Fig. S2C**]. The fEPSPs in the AIR
177 and 0.1 mM D-βHb groups were generally comparable. The FVs remained statistically similar
178 among all the groups, with approximately the same response pattern [**Fig. S2E-G**], replicating the
179 results in Fig. 1 and Fig. S1.

180 Taken together, these results strongly suggest that the effects of AIR and/or D-βHb could differ
181 among cellular compartments (i.e., dendritic versus somatic) and have different specificities for
182 various cellular compartments, with synapses being particularly susceptible to the metabolic
183 challenges induced by GLUT4 inhibition.

184

185 *4.2 AIR impairs axonal conduction speeds, but D-βHb treatment restores and enhances axonal*
186 *conduction in a dose-dependent manner.*

187 In the previous sections, we highlighted how AIR and D-βHb affected fEPSPs and FVs, finding a
188 surprising lack of adverse effects of AIR on FV amplitudes and a noticeable reduction in fEPSP
189 amplitudes, with the effects further exacerbated by D-βHB. This difference suggests that AIR
190 and/or D-βHb treatment might have differential effects on cellular compartments. We then
191 investigated whether other axonal properties changed during AIR and whether D-βHB application
192 remedied such changes.

193 We found that inducing AIR resulted in a strong reduction in the conduction velocities (CVs) of
194 SCOs [**Fig. 2C**; -13.07 ± 2.87% Control vs. AIR, p=0.027]. After the addition of 0.1 mM D-βHb
195 during AIR, the CV recovered to control levels [**Fig. 2C**; +12.43 ± 4.42% AIR vs. 0.1 mM D-
196 βHb+AIR, p=0.034; +0.01 ± 0.07% Control vs. 0.1 mM D-βHb+AIR, p=0.99], and the application
197 of 1 mM D-βHb significantly improved the CV, surpassing the control level [**Fig. 2C**; +31.79 ±
198 4.59% for AIR vs. 1 mM D-βHb+AIR, p=4.2E-8; +19.10 ± 4.53% for control vs. 1 mM D-βHb+AIR,
199 p=0.00057].

200 To better interpret these findings, we constructed a computational model of the CV by employing
201 an approximation of axonal cable theory (see Methods). Our model examined three processes
202 that determine the CV: the resting membrane potential (V_R), peak membrane potential (V_A, the
203 amplitude of AP overshoot), and activation threshold potential (V_T, potential for Na_v activation).
204 We considered V_T to be robust to various physiological conditions, as this value primarily depends
205 on the Na_v channel type and gating kinetics [39]; therefore, we fixed V_T at a constant value of -50

206 mV in our calculations. We varied V_R between -90 and -60 mV and V_A between 10 and 30 mV,
207 both of which are considered typical physiological ranges. We normalized the results according
208 to a reference state with V_R = -75 mV, V_A = 30 mV, and V_T = -50 mV. The modeling results showed
209 that decreased CV was associated with either hyperpolarized resting membrane potential or
210 decreased peak AP amplitude [**Fig. 2F-G**].

211

212 *4.3 AIR adversely affects input timing, which is restored by high D-βHb concentrations.*

213 Changes in the CV magnitude and the resulting differences in the input timing would likely
214 desynchronize the hippocampal circuit. Therefore, we investigated whether the latency of FVs
215 changes during stimulation with 20 pulse trains.

216 In all treatment groups, the early FVs showed ~-0.2 ms improvement in latency. During the first 3
217 min, all experimental groups were comparable and exhibited the same pattern of latency changes.
218 Afterward, the AIR and 0.1 mM D-βHb+AIR groups displayed progressively more prominent
219 delays than the Control group, while the Control and 1 mM D-βHb+AIR groups remained
220 comparable. During AIR, we observed the largest delays [**Fig. 3E-F, Fig. 3I, L**; at 15 min, stim. 9-
221 11: +2.69 ± 0.84 ms, Control vs. AIR, p=0.0077; 2.64 ± 0.94 ms, AIR vs. 1 mM D-βHb+AIR,
222 p=0.020]. The increased delays during the stimulation suggest that the detrimental effects of AIR
223 are exacerbated over longer periods.

224 *4.4 AIR increases membrane resistance (R_m) without affecting other intrinsic membrane*
225 *properties of CA1 pyramidal neurons, and D-βHb treatment during AIR does not rescue R_m to*
226 *normal levels.*

227 The above results [**Fig. 2**] indicate that AIR might negatively impact the membrane properties of
228 hippocampal neurons; therefore, we sought to identify the properties most vulnerable to AIR and
229 test D-βHb as a recovery agent. Based on the dose–response results from the field potential
230 studies, we selected 1 mM D-βHb for use in patch-clamp experiments, testing the effects of AIR
231 and D-βHb on the intrinsic membrane properties of CA1 pyramidal neurons (membrane
232 resistance, R_m; membrane capacitance, C_m, and resting membrane potential, V_{rest}) and their spike
233 thresholds. We found that the R_m of the CA1 pyramidal neurons in the AIR group was significantly
234 increased compared with that of the neurons in the control group [**Fig. 4B**, +43.24 ± 3.73%,
235 p=1.41E-07], and this increased value was observed even with the application of 1 mM D-βHb
236 [**Fig. 4B**, +27.86 ± 8.93%, p=0.030], while the results in the AIR and 1 mM D-βHb+AIR groups
237 were similar (p=0.31). Interestingly, neither the C_m [**Fig. 4C**, 114.25 ± 9.73, 115.52 ± 9.26, 132.20
238 ± 9.46, Control, AIR, D-βHb+AIR, respectively, p=0.32], spike threshold [**Fig. 4E**, -46.31 ± 0.76, -
239 44.53 ± 0.80, 44.64 ± 0.73, p=0.17] nor $V_{rest.}$ [**Fig. 4F**, -67.26 ± 1.17, -63.57 ± 1.38, -65.11 ± 0.99,
240 p=0.093] were significantly affected by either the AIR or D-βHb+AIR treatments.

241

242 *4.5 AIR increases the frequency of spontaneous vesicular release at CA1 synapses (sEPSCs)*
243 *and mildly increases sEPSC amplitudes. D-βHb does not reverse the increase in frequency but*
244 *mildly decreases sEPSC amplitudes.*

245 Recovering the membrane back to the resting potential during synaptic transmission is the most
246 energy-consuming neuronal process (~% of total ATP produced [40]); therefore, we investigated
247 changes in the frequency and magnitude of quantal EPSCs that might explain the ~35% decrease
248 in fEPSP amplitudes reported above [**Figs. 1-3**].

249 AIR significantly increased the frequency of spontaneous synaptic currents (sEPSCs), with
250 approximately twice as many events observed in the AIR group than in the control group [**Fig.**
251 **5A, B**; 0.53 vs. 0.96 Hz, +0.42 ± 0.12 Hz, p=0.0031]. Interestingly, D-βHb failed to rectify the
252 increased qEPSC frequency [**Fig. 5A, B**; D-βHb+AIR 0.93 vs. AIR 0.96 Hz, 0.021 ± 0.15 Hz,
253 p=0.99; D-βHb+AIR vs. Control, +0.40 ± 0.12 Hz, p=0.0091]. However, the amplitude, rise time,
254 and sEPSC decay time did not differ significantly among the groups [**Fig. 5C-E**].

255 Given the change in R_m, the lack of significant changes in the amplitudes is surprising. Several
256 studies utilizing different metabolic states, such as food deprivation [41] and inhibition of glycolysis
257 [42], showed increased mEPSC/sEPSC amplitudes; therefore, we decided to investigate the
258 sEPSCs in more detail. In most central synapses, the distribution of mEPSC/sEPSC amplitudes
259 shows several peaks related to the simultaneous release of multiple neurotransmitters [43], with
260 each subsequent peak linked to an increasing number of concurrent sEPSCs. According to the
261 multiplicative nature of this process, we assumed that small changes in amplitudes [**Fig. 5E**]
262 would scale up. We detected 2-4 distinct peaks in ~85% of the analyzed cells [**Fig. S3A-C**], with
263 no differences in the number of cells with multipeak distributions among the groups [**Fig. S3C**;
264 89.5% in Control; 84.2% in AIR, 87.5% in D-βHb+AIR]. In line with our initial assumptions, the
265 scaled amplitudes revealed differences among the groups [**Fig. S3E**]: the amplitudes in the AIR
266 group were significantly higher than those in the D-βHb+AIR group [p1: p=0.048; p2: p=0.0054;
267 p3: p=0.0038; p4: p=0.021] and differed from those in the control group at peak 3 [p=0.007]. The
268 Control and D-βHb+AIR groups did not show significant differences at any point [**Fig. S3E]**,
269 despite the same sEPSC frequency as in the AIR group.

270 We validated these findings by comparing the normalized amplitude distributions among the
271 different groups [**Fig. S3F-I**]. Within the range correlating to peaks 2–4 (sEPSC of ~20 pA or
272 greater), significantly more large events were observed in the AIR group (15.19% of total) than in
273 the control (7.65%) or D-βHb+AIR (9.48%) groups [**Fig. S3F-I**], while the results in the control and
274 D-βHb+AIR groups were essentially comparable. This result suggests that during AIR, the
275 elevated frequency of events increased the probability of multivesicular events occurring, which
276 was further exacerbated by the ~20% increase in R_m. On the other hand, D-βHb+AIR produced a
277 distribution resembling the control, as if the vesicles had lower glutamate content, as suggested

278 by the literature [44,45].

279

280 4.6 *AIR slightly changes the firing pattern of hippocampal pyramidal neurons and causes*
281 *increased membrane depolarization with input. These effects are reversed by D-βHb, which also*
282 *increases AP amplitudes.*

283 The AP generation and subsequent recovery of V_m to resting levels require a large part of the
284 energy budget of pyramidal neurons (~41% of all produced ATP [40]). Therefore, we investigated
285 whether pyramidal neurons retain their input–output curves (I-O curve) during AIR and how D-
286 βHb alleviates AIR effects.

287 First, we focused on the firing frequency [**Fig. 6A**]. Cells in the AIR group showed increased firing
288 at lower current injections than those in the D-βHb+AIR group [**Fig. 6B**, 75–150 pA, p=0.0038 to
289 0.050], but with the same maximal firing rate. These results suggest that the cells activate earlier
290 in the AIR condition than in the control or D-βHb+AIR conditions. To test this further, we measured
291 the maximum depolarization obtained by each neuron during the final 5 ms of each current
292 injection step [**Fig. 6D**]. AIR neurons had slightly higher depolarization with each injection step
293 compared to control neurons [**Fig. 6E, F**; p=0.0027 to 0.048] or D-βHb+AIR [**Fig. 6E, F**; p=0.0029
294 to 0.042].

295 Next, we investigated the average AP peak amplitudes [**Fig. 6G**], per step [**Fig. 6H**]. Surprisingly,
296 D-βHb+AIR neurons showed larger amplitudes, which were consistently elevated throughout the
297 injection period, than control or AIR neurons, while AIR neurons remained comparable to control
298 neurons [**Fig. 6I**, p=0.0017 to 0.036, AIR vs. Control; p=0.0093 to 0.044, AIR vs. 1 mM D-
299 βHb+AIR].

300 4.7 *AIR increases the AP decay time, while D-βHb accelerates the AP rise time without reversing*
301 *the AIR-induced slower AP decay.*

302 We next proceeded to investigate other AP properties: the decay time (from the overshoot peak
303 to 0 mV) [**Fig. 7A-C**] and rise time (from 0 mV to the overshoot peak) [**Fig. 7D-F**]. We found that
304 control neurons had significantly lower average AP decay times than AIR [**Fig. 7B, C**; p=0.047 to
305 0.0019] and D-βHb+AIR neurons [**Fig. 7B, C**; p=0.041 to 0.0023] for almost all current injection
306 steps. Moreover, AIR and D-βHb+AIR cells did not significantly differ at any point [**Fig. 7B, C**;
307 p=0.32 to 0.99]. D-βHb+AIR cells demonstrated faster rise times than control cells [**Fig. 7E, F**;
308 p=0.000094 to 0.0025] and AIR cells [**Fig. 6E, F**; p=0.047 to 0.0052] for most injection steps.
309 Interestingly, AIR cells exhibited slightly faster AP rise times exclusively at the lowest current
310 injection times [**Fig. 4N, O**; p=0.012 to 0.035]. These slightly faster APs were likely due to earlier
311 activation of the cells, as shown in [**Fig. 6B-C, E-F**].

Finally, as we did not observe significant differences in the firing frequency among the groups [**Fig. 6B, C**], we examined variations in the timing of AP firing based on the intervals between consecutive APs (AP interevent interval, AP IEI) [**Fig. 7G**], but we did not observe obvious changes in the AP IEI [**Fig. 7H, I].**

4.8 *AP adaptation is impaired during AIR, with AP amplitudes showing steeper declines, and is not reversed by D-βHb.*

The AP overshoot amplitudes, decay times, and rise times demonstrated steeper slopes in the AIR and D-βHb+AIR groups than in the control group. The AP properties during neuronal firing undergo dynamic changes, commonly referred to as spike adaptation or spike-frequency adaptation [46], and in our experiments, we observed that GLUT4 antagonism intensified these changes.

To test this observation, we compared the peak amplitudes of the first APs [**Fig. S4A-D**], the averaged APs [**Fig. 6G-I**, **Fig. S4E**] and the final APs during current injections [**Fig. S4F**]. The first APs represent neuronal firing after rest (10 s between subsequent injections), while the average and final APs represent firing after energy expenditure. As expected, the first APs displayed minimal changes in amplitude during injections [**Fig. S4D**], with larger amplitudes observed in the D-βHb+AIR group than in the control group. Moreover, although elevated amplitudes were observed in the AIR group, the results did not differ significantly from those in the control or D-βHb+AIR groups. For the final APs, we observed a sharp decline in amplitude, which scaled with the injected current [**Fig. S4F**], in both the AIR and D-βHb+AIR groups. Lower amplitudes were observed in the control group than in the D-βHb+AIR group for 100-300 pA injections ($p=0.040$ to $p=6E-05$), and the results remained comparable to those in the AIR group until the final, large, 400-500 pA injections ($p=0.032$ to $p=0.0011$), when the APs in the AIR group decreased significantly [**Fig. S4F**]. The results in the AIR and D-βHb+AIR groups remained consistently different. Linear fits to the average AP amplitudes revealed significantly steeper declines in the AIR and D-βHb+AIR groups [**Fig. S4G, H**; $p=0.00039$, AIR vs. Control; $p=0.0012$, D-βHb+AIR vs. Control], indicating that prolonged neuronal activity is heavily affected by AIR and D-βHb does not provide direct recovery.

4.9 *Changes in AP decay and rise times correspond to differences in the widths of FVs.*

In our initial analysis of the field potential (FV) data, we focused on the amplitudes of the biological signals. Consistently, we found no significant changes in the FV amplitudes [**Figs. 1F, 2C, 3E-G**], which supports our findings on AP overshoot amplitudes [**Fig. 6G-I**] (except in the D-βHb+AIR group). Based on these results, we investigated whether the changes in the AP decay and rise

347 times corresponded to changes in the FV widths during train stimulation [**Fig. S5**].

348 Consistent with our findings on AP decay/rise times [**Fig. 7A-F**], the widest FVs during the
349 stimulation were consistently observed in the AIR group, followed by the control group, with the
350 narrowest FVs observed in the 1 mM D-βHb+AIR group [**Fig. S5D**]. We found differences between
351 the AIR and control groups (p=3.94E-06 to 0.049) and AIR and 1 mM D-βHb+AIR groups
352 (p=4.04E-05 to 0.046) throughout the whole stimulation period, while the results in the control and
353 1 mM D-βHb+AIR groups were not different (p=0.079 to 0.99), supporting our AP decay/rise time
354 findings [**Fig. 6G-I**].

355

356 4.10 *With abolished GABAergic inhibition, AIR strongly decreased the firing rates of CA1*
357 *pyramidal neurons and fast-spiking interneurons (FSIs), which were not rescued by D-βHb.*

358 We next investigated the properties of CA1 pyramidal neurons and FSIs after pharmacologically
359 abolishing AMPA/kainate excitatory (NBQX) and fast GABAergic inhibitory (gabazine)
360 transmission [**Fig. S6**].

361 We first recorded the firing frequency of CA1 pyramidal neurons [**Fig. S6A, B**] at different
362 activation levels [**Fig. S6C, D**] and found that AIR prominently decreased their firing rate when
363 compared with the control [**Fig. S6C**, p=0.024 to 0.0053]. Surprisingly, the application of 1 mM D-
364 βHb during AIR resulted in a stronger reduction in the firing rate than in the control group [**Fig.**
365 **S6E**, p=0.000027 to 0.035]. The AIR and D-βHb+AIR results remained similar throughout the
366 injections [**Fig. S6E**]. However, all groups differed significantly with respect to the maximum firing
367 rate, with the highest firing rate observed in the control group (31.03 ± 3.43) and the lowest firing
368 rate observed in the D-βHb+AIR group (13.17 ± 2.05).

369 Next, we examined CA1 FSIs using the same drug conditions [**Fig. S6E, F**]: AIR decreased the
370 firing rate of FSIs compared with the control [**Fig. S6G**, p=0.012 to 0.048], which was not reversed
371 by D-βHb [**Fig. S6H**, p=0.00017 to 0.035]. For pyramidal neurons, the FSIs in the AIR and D-
372 βHb+AIR groups remained mostly comparable [**Fig. S6G**]. None of the groups differed in the
373 maximum firing rate [**Fig. S6H**, p=0.068].
374 3.11 The *Hodgkin-Huxley model predicts that impairments in Na^+/K^+ ATPase activity result in*
375 *more depolarized V_{rest}, lower AP overshoot (V_a), and increased neuronal firing.*

376 Here, we aim to explain the previous observations of dysregulated firing dynamics in response to
377 AIR. We hypothesize that indinavir restricts the energy supply of neurons and thus impairs the
378 neuronal Na^+/K^+ ATPase. To test this hypothesis, we developed a computational model of an
379 isolated CA1 neuron in the absence of inhibition and toggled Na^+/K^+ ATPase activity through the
380 enzyme kinetic parameter v_{ATPase}^{max} (see Supplementary Methods, **Fig. S7**). **Fig. S7A, B** (at two
381 different temporal scales) shows the predicted changes in neuronal firing dynamics when the

382 Na^+/K^+ ATPase is impaired. This impairment predicts the depolarization of the resting membrane
383 potential [**Fig. S7C**] and is consistent with the trends of our I/O curves [**Fig. 4F**]. Furthermore, in
384 this depolarization model, the magnitude of the membrane potential shift needed for an AP is
385 reduced. Consequently, the model predicts increased firing frequency [**Fig. S7D**]. Finally, the
386 model predicts that the Na^+/K^+ ATPase should act more slowly to recover ion gradients after an
387 AP, causing the amplitudes of the subsequent APs to decline progressively with time [**Fig. S7E,**
388 **F**]. This amplitude decrease is consistent with the trends in the measured CV [**Fig. 2**].

389

390 5. **Discussion**

391 Central insulin resistance impairs cognitive performance and promotes hippocampal
392 neurodegeneration and memory loss [47,48]. Our present results highlight the adverse effects of
393 GLUT4 inhibition on synaptic function and LTP, in accord with findings that acute and chronic
394 blockade of GLUT4 are detrimental to hippocampus-mediated memory tasks, thus suggesting
395 that GLUT4 is critical for the acquisition and consolidation of memory [8,13]. Memory formation
396 promotes GLUT4 incorporation into the membrane, resulting in increased glucose flux into
397 neurons [13,49]. This process enables increased metabolic support during high-demand
398 activities. Crucially, most GLUT4s localize in the perikaryon [50,51], likely near axosomatic
399 synapses, which are associated with synaptic plasticity and long-term memory (LTM). Indeed,
400 prolonged blockade of GLUT4 glucose transporters in the brain results in impaired formation of
401 LTM [13] and decreased levels of hippocampal BDNF [52]. Moreover, hypoglycemia negatively
402 affects memory performance and cognition [53,54; however, see 13].

403 In this study, we found that AIR increased the frequency of sEPSC events, in line with previously
404 published data showing similar increases during food deprivation [42], inhibition of glycolysis [41]
405 and ischemia [55], likely due to hypoglycemia-driven Ca^{2+} accumulation at presynaptic terminals
406 [41,55]. These studies also suggest that presynaptic glycolysis is essential for maintaining
407 synaptic transmission, even at low frequencies, and that mitochondrial respiration cannot
408 compensate for these effects. Normally, glycolysis requires approximately one-third of the energy
409 used at presynaptic terminals, thus sustaining low-frequency transmission. In addition, impaired
410 glycolysis leads to slower, broader, and smaller AP waveforms and depolarization of the resting
411 membrane potential [42], which is consistent with our results. Interestingly, D-βHb+AIR treatment,
412 which showed the same increase in the frequency of sEPSC events as AIR, led to the lowest
413 sEPSC amplitudes [**Fig. S3E**]. This result suggests a reduction in the number of synaptic vesicles
414 and is consistent with reports of reduced conversion of glutamate to aspartate during ketosis
415 [44,45].

416 Although the results of our computational models are consistent with the observed changes in the
417 resting-state membrane potential and firing frequency during AIR, there were seemingly
418 contradicting results with respect to the AP peak amplitude. Specifically, we found no significant

419 changes in the average AP overshoot amplitudes during AIR, and our model predicted a decrease
420 due to energy constraints. In the model, we did not consider a progressive decline in available
421 energy, which is suggested by the steeper AP adaptation [**Fig. S4**]. Moreover, neurons may
422 compensate for such energetic limitations by increasing R_m (as reported in 42), while our model
423 assumes that R_m remains unchanged. When those factors are accounted for, the model and
424 experimental data agree: during periods of extensive activity, energy reserves in neurons are
425 progressively depleted and, provided that the neuron rapidly fires multiple APs, the negative
426 effects of hypoglycemia overcome compensatory R_m increases; then, the AP amplitudes
427 decrease below control levels [**Fig. S4**]. Furthermore, we used the maximal Na^+/K^+ ATPase
428 activity to represent ATP availability and considered literature estimates of kinetic and
429 thermodynamic rate constants. A more direct approach might consider ATP concentration as an
430 input variable, in cases in which such experimental data are available.

431 Our model aims to establish the underlying causes of the changes in CV, and we investigated
432 resting membrane potential (V_{rest}) and AP peak amplitude as two critical factors. The model
433 explains CV recovery and increases during D-βHb+AIR treatment, as the measured AP peak
434 amplitudes remain consistently elevated and V_{rest} changes are negligible, but fails in the case of
435 AIR alone, with the AP amplitudes remaining comparable to the control levels and V_{rest} tending to
436 depolarize. This discrepancy might reflect the simplistic nature of our model, which neglects
437 complex ion dynamics, altered membrane permeability and synaptic processes.

438 The ketogenic diet has been used to treat epilepsy for decades and has been considered in many
439 therapeutic applications [30]. Possible mechanisms include modulation of ATP-sensitive K^+
440 channels (K_{ATP}), free fatty acid receptor 3 (FFAR3/GPR41) activation, promotion of GABA
441 synthesis, and epigenetic modifications [56]. The action of D-βHb in modulating potassium flux
442 through K_{ATP} channels may be most relevant in the present context [57] since K_{ATP} activation
443 results in decreased neuronal firing rates [58,59] and prevents picrotoxin-induced epileptiform
444 activity in the hippocampus [60]; thus, this action may explain the present findings that firing rates
445 and membrane depolarization remained at control levels in the presence of 1 mM D-βHb during
446 AIR (despite elevated R_m).

447 D-βHb is a precursor of glutamine, which promotes increased GABA levels, as seen in studies on
448 the ketogenic diet in patients with epilepsy [61]. D-βHb also directs glutamate toward GABA
449 production by reducing the conversion of glutamate to aspartate [44,45]. In addition, D-βHb
450 directly affects the vesicular glutamate transporter VGLUT2 by inhibiting Cl^- dependent glutamate
451 uptake. VGLUT2 is critical for glutamate excitatory transmission in CA3-CA1, and conditional
452 VGLUT2 knockout results in impaired spatial learning and reduced LTP [62]. Together with the
453 increased formation of GABA and/or GABA derivatives, VGLUT2 inhibition could reduce
454 glutamate excitatory transmission [63].

455 The present results have important implications for the treatment of conditions such as type 2
456 diabetes, metabolic syndrome, and seizure disorders that involve insulin hyposensitivity.

According to NIH estimates, ~30% of Americans display symptoms of prediabetes, and this percentage is expected to increase. With longer average lifespans and demographic changes leading to an increase in the aging population, obtaining insights into the outcomes of metabolic dysfunction and its potential treatment has become a crucial issue. Our results provide unique insight into the potential use of KBs as an inexpensive and relatively risk-free treatment for metabolic disorders and insulin resistance. Medical researchers can use this information to discover new targets for treatment and develop more effective therapies. Further research in this area could inform novel treatment approaches that address the complex effects of metabolic disorders on brain health.

6. **Materials and Methods**

6.0 *Mice*

Breeding pairs of transgenic GAD2Cre/GCamp5gTdTomato, Thy1/GCamp6fTdTomato, and C57BL/6J mice were originally obtained from The Jackson Laboratory (stocks 010802, 024477, 024339) or Charles River Laboratories and bred in-house under standard conditions of a 12-12 hour light-dark cycle, with food and water available *ad libitum*. The Institutional Animal Care and Use Committee approved all experiments. Mice of both sexes aged between 30 and 60 days (P30-P60) were used in all experiments.

6.1 *Electrophysiology – slice preparation.*

Coronal brain slices containing the hippocampus were used in all recordings. Mice were deeply anesthetized with a mixture of isoflurane and air (3% v/v) and decapitated, and their brains were extracted and cut using a Leica VT1200S vibratome into 300 µm-thick slices in ice-cold ACSF solution containing (in mM): 230 sucrose, 1 KCl, 0.5 $CaCl_2$, 10 $MgSO_4$, $NaHCO_3$, 1.25 NaH_2PO_4, 0.04 Na-ascorbate, and 10 glucose; 310 ± 5 mOsm, pH adjusted to 7.35 ± 5 with HCl, and gassed with carbogen (95% O_2, 5% CO_2) for at least 30 min before use. The slices were then transferred to a Zbicz-type BSC-PC submerged slice chamber (Harvard Apparatus, USA) filled with artificial cerebrospinal fluid (ACSF) containing (in mM): 124 NaCl, 2.5 KCl, 2 $CaCl_2$, 2 $MgSO_4$, 26 $NaHCO_3$, 1.25 NaH_2PO_4, 0.04 Na-ascorbate, and 10 glucose; 305 ± 5 mOsm/kg, pH adjusted to 7.35 ± 0.05 mOsm/kg, gassed with carbogen and prewarmed to 32 °C. The slices were allowed to recover in warm ACSF for 15 min; then, the heating was switched off, and the chamber was gradually cooled to room temperature (RT; 23 ± 2 °C) over 45 min.

Following recovery, individual slices were transferred to another BSC-PC chamber filled with gassed ACSF and a mixture of drugs (indinavir 0.1 mM; indinavir 0.1 mM and either 0.1- or 1-mM D-βHb), where they were incubated for 60 ± 15 min. Next, the slices were transferred to a

492 submerged recording chamber mounted on an upright microscope stage (E600FN, Nikon, Japan)
493 equipped with infrared differential interference contrast (IR-DIC) filters. The slices were kept at
494 RT and superfused continuously with gassed ACSF delivered by a peristaltic pump at a steady
495 rate of ~2 ml/min.

496

497 6.2 *Field potential recordings.*

498 Evoked field potential responses were triggered with an isolated pulse stimulator (Model 2100,
499 AM Systems, USA) using a CBARC75 concentric bipolar electrode (FHC, USA) placed between
500 CA3 and CA1. The recording electrode was placed 300 ± µm away from the stimulation electrode
501 for the CA1 FV and fEPSP recordings. During the axonal conduction velocity (CV) recordings, the
502 electrodes were spaced 300 to 900 ± 50 µm apart, and up to 6 different sites were recorded. All
503 stimulation paradigms were applied every 20 s as biphasic rectangular pulses with a total duration
504 of 240 µs, 50 ± 5 V strength (~60 ± 10% of the maximum response size), and a between-stimuli
505 frequency of 25 Hz (40 ms).

506 During non-CV recordings, three different types of stimulation were applied: paired, 20 stimuli,
507 and stimuli trains, repeated every 20 s for a total period of 20 min in each case. After each train
508 stimulation, the slice was allowed to recover for 20 min under paired stimulation conditions.

509 Recording pipettes were pulled from borosilicate glass capillaries (ID 0.86, OD 1.5, BF1-86-10,
510 Sutter Instruments, USA) with a vertical PC-100 puller (Narishige, Japan) and filled with 6% NaCl
511 (in H_2O, 1.02 M). Only pipettes with a resistance of 0.2-1.0 MΩ were used. Recording pipettes
512 were allowed to rest at the recording site for 10 min to equilibrate before the start of a recording.
513 All recorded signals were acquired using a MultiClamp 700B amplifier (Molecular Devices, USA),
514 Bessel-filtered at 2 kHz, and digitized at a sampling frequency of 10 kHz using an Axon Digidata
515 1440A digitizer (Molecular Devices, USA).

516

517 6.3 *Whole-cell patch-clamp recordings.*

518 Pyramidal neurons in the hippocampal CA1 region were selected for recordings based on their
519 general morphology and position within the pyramidal layer. As an additional verification, recorded
520 cells were screened for $GAD2^+$-driven tdTomato fluorescence. Cells that displayed any level of
521 tdTomato fluorescence were rejected.

522 Patch pipettes were pulled from borosilicate glass capillaries (BF1-86-10, Sutter Instruments,
523 USA) with a vertical puller (PC100, Narishige, Japan). Pipettes had a resistance of 6–8 MΩ when
524 filled with an internal solution containing (in mM): 136 K-gluconate, 4 Na_2ATP, 2 $MgCl_2$, 0.2 EGTA,
525 10 HEPES, 4 KCl, 7 di-triphospho-creatine, 0.3 Na_3GTP; 280–290 ± 5 mOsm/kg, titrated to pH

526 7.3 ± 0.05 with KOH.

527 During the voltage clamp (VC) recordings, cells were clamped at a holding potential (V_h) of −70
528 mV with a Multiclamp 700B amplifier (Molecular Devices, USA). The liquid junction potential was
529 not corrected. The pipette capacitance was compensated for in all recordings. During VC
530 experiments, the series resistance (R_s) was not compensated. During the current clamp (CC)
531 recordings, a holding current was applied to the cells to maintain the membrane potential at V_h =
532 -70 ± 3 mV. All cells were bridge-balanced at 50 % of R_s. The cell capacitance was not
533 compensated for in either mode. Immediately after establishing the whole-cell configuration, the
534 cell was kept in I=0 mode to monitor the resting membrane potential (V_{rest}) over a period of ~120
535 to 180 s. The average value of V_{rest} over this period is reported as the neuron's V_{rest}.

536 During the recordings, every 5 to 10 min, a series of 10 square voltage steps of −10 mV was
537 applied to monitor changes in R_s (V_h = -70 mV). All whole-cell currents in response to voltage
538 steps were low-pass filtered at 10 kHz with a Bessel filter and sampled at 20 kHz frequency (Axon
539 Digidata 15B, Molecular Devices, USA). For inclusion in the final dataset, recordings had to meet
540 3 criteria: 1) The R_s value after any recording protocol could not be more than 20% larger than
541 the R_s value before the protocol; 2) the R_s value during any of the recording protocols could not
542 exceed 30 MΩ; and 3) the offset drift by the end of the recordings could not be higher than ± 5
543 mV.

544 Spontaneous synaptic currents (sEPSCs) were recorded in VC at V_h = -70 mV, in a single,
545 continuous sweep for 10 to 15 min, low-pass filtered at 2 kHz with a Bessel filter and sampled at
546 10 kHz frequency.

547 To establish the spiking threshold, each neuron was current-clamped at V_h ~ -70 ± 3 mV and
548 subjected to a ramp-shaped 200-500 pA current injection with a 1 s duration. The spike threshold
549 was determined as the membrane potential at which the first fully developed action potential (AP)
550 was visible. Each ramp injection was repeated 10x, and the averaged threshold value is reported
551 for the neuron.

552 To establish the firing properties of the recorded neurons, each neuron was current-clamped as
553 described previously and subjected to a series of square current injections with a change of 25
554 pA per step to a maximum of 0 pA, with each step having a 1 s duration and an interstep interval
555 (ISI) of 10 s. If necessary, the holding current was corrected during the protocol to maintain V_h at
556 ~ -70 ± 3 mV. During analyses, only fully formed APs that crossed the 0 mV threshold were
557 included.

558 All data acquisition was performed using pCLAMP software (Molecular Devices, USA).

559

560 6.4 *Field potential recordings – analyses.*

561 During field potential recordings, the biologically relevant signals are superimposed onto the
562 decaying stimulation artifact. To isolate the stimulation artifacts for subtraction from the signal at
563 the end of each recording, we applied 1 μM TTX to the slice and recorded 30 repetitions of each
564 stimulation paradigm in the presence of TTX.

565 Recorded traces were analyzed in Igor Pro (Wavemetrics, USA). First, an average of the traces
566 recorded with TTX was subtracted from each trace. The traces were then filtered using a rolling
567 five-point average to remove noise, and the baseline was adjusted to the 1 s period before the
568 stimuli. The amplitudes and latencies of the FVs and fEPSPs were measured at their peaks.
569 Amplitudes were measured against 0 mV baselines, while latencies were measured against the
570 onset of the stimulation. During high-frequency stimulation, cells often do not have sufficient time
571 to fully recover their membrane potentials before the next stimulus is applied, leading to a gradual
572 shift in the baseline; therefore, as a correction, we subtracted the median voltage at +35 to +40
573 ms after each stimulus from each FV or fEPSP amplitude. FV widths were measured at the peaks
574 of positive deflections in the waveform, with the first peak after the artifact subtraction and the
575 second peak directly before the fEPSP.

576 All traces were screened for occasional electrical interference, and the affected data points were
577 manually removed from the analysis.

578 To measure the axonal conduction velocity (CV), we calculated the time shift (Δt, ms) between
579 the stimulus start and the time of the FV peak. Next, the linear distance between the recording
580 site and the stimulation electrode was divided by the measured Δt. We recorded CV values at 3-
581 6 sites over a span of 300-900 μm, with ~1 μm steps between sites. Each CV recording site
582 served as a replicate for statistical analysis (see Statistics). During CV recording, the stimulation
583 site remained stationary, and the sites were recorded in randomized order.

584 To calculate changes in the FV peak latency during train stimulations, the median Δt for stimuli 1-
585 3 and traces 1-2 (Δt_N) was subtracted from each Δt (normalization).

586

587 6.5 *Field potential recordings – data visualization.*

588 To construct "heatmap" visualizations of the data, numerical matrices of the FV or fEPSP
589 amplitude means were built for each of the four treatment groups. In every matrix, each new row
590 represented responses during each subsequent train. Then, two additional columns were added
591 at the end as a color normalization in the heatmap (0, 1 mV), and the matrix was saved as a text
592 file. Next, the text files were imported as text images to ImageJ (NIH, USA), converted from 32-
593 to 16-bit, saved as TIFF images and imported into Igor Pro (Wavemetrics, USA); then, their look-
594 up table (LUT) was changed from "Grays" to "Spectrum."

595 The heatmaps for latency changes during train stimulation were generated similarly but using

596 different normalizations: the 20 pulse train recordings had normalization boundaries of -1 and +1
597 ms.

598

599 6.6 *Whole-cell patch-clamp – sEPSC analyses.*

600 sEPSC detection was automatized using a convolution-based algorithm in Fbrain 3.03 [64], a
601 customized program in Igor Pro 6 (WaveMetrics, Lake Oswego, USA), kindly provided by the
602 Peter Jonas Lab (IST, Klosterneuburg, Austria). Recorded traces were smoothed by subtracting
603 a 20-term polynomial fitted to the trace and digital notch (60 ± 0.5 Hz) filtered in FBrain before the
604 analysis. The convolved trace was passed through a digital bandpass filter at 0.001 to 200 Hz.
605 The event detection template had a rise-time constant τ = 1.5 ms, a decay τ = 6 ms, and an
606 amplitude of −10 pA. The event detection threshold (θ) was set to 4.2 times the standard deviation
607 of a Gaussian function fitted to the all-point histogram of the convolved trace. All events detected
608 by the algorithm were inspected visually. Events that clearly did not show the fast rise times and
609 exponential decay kinetics of a typical hippocampal EPSC were manually removed. Only cells
610 with a rejection ratio lower than 20% were included in the analysis. The analysis was performed
611 using custom-written macros provided by Dr. Maria Kukley (Achucarro Basque Center for
612 Neuroscience, Bilbao, Spain).

613 Afterwards, individual sEPSC waveforms were extracted from the trace. Each waveform
614 consisted of a 5 ms segment of the trace before the onset of the sEPSC and a 50 ms segment
615 after the sEPSC onset to capture the full decay of the waveform. Before averaging, all sEPSCs
616 were baseline-adjusted to the pre-onset time by 5 ms. The peak amplitude, 20-80% onset-to-peak
617 rise time, and decay constant τ were measured for the averaged sEPSCs. The decay constant τ
618 was calculated from the monoexponential fit from the sEPSC peak to the final ms of the averaged
619 waveform.

620 To avoid selection bias during sEPSC extraction, we repeated the Fbrain analysis at least twice
621 for each cell and averaged the results.

622

623 6.7 *Statistics.*

624 All data were acquired in randomized sequences, with a maximum of 2 slices (field potential
625 recordings) or 2 cells (patch-clamp recordings) from a single animal per experimental condition
626 to avoid pseudoreplication. All experimental groups had comparable distributions of ages (close
627 to P50 ± 6) and sex. The order of slice preincubation with drugs was randomized for each animal.
628 The numbers of slices or cells and animals used in each experiment are indicated in the figure
629 legends.

Statistical analysis was performed using GraphPad Prism 9.5.1 (GraphPad Software, USA). Significant outliers were removed with the Prism ROUT method at Q = 5%, and the normality of residuals and homoscedasticity were tested for each comparison. If the datasets had normal residuals and equal variances, we used ordinary one-way ANOVA with *post hoc* Holm-Šídák's test. If the datasets had normal residuals but unequal variances, we used Brown-Forsythe ANOVA with *post hoc* Dunnett's T3 test. If the datasets were not normally distributed but had equal variances, we used Kruskal–Wallis ANOVA with *post hoc* Dunn's test. In rare cases where the data were neither normally distributed nor had equal variance, we applied Brown-Forsythe ANOVA with *post hoc* Dunnett's T3 test. If the dataset consisted of multiple replicates, we used nested one-way ANOVA with *post hoc* Holm-Šídák's test. The tested groups and p values are indicated in the text or the figure legends. Individual cells or slices are labeled n, replicates are labeled m, and the numbers of animals used are labeled N. If the groups tested are different, we report the p values of *post hoc* tests but omit the p value of the omnibus test. If the groups did not test as different, only the p value of the omnibus test is reported. For scatter plots, each point represents an individual data point (cell, slice, or replicate), and the horizontal bars represent the group mean ± SEM. In all other graphs, we present the mean ± SEM. The heatmaps represent the group means.

6.8 *Model of conduction velocity*

Here, we model how the AP shape affects the conduction velocity (CV) along an unmyelinated axon. We model an infinitesimally small unit of the axon consisting of three distinct units in a row, separated by a space h. The first and last of these units are kept "fixed" at voltages $V_1 = V_a$ (the peak membrane potential) and $V_3 = V_{rest}$, respectively; this potential difference leads to a voltage flow across the axon, which is generally described by the cable equation [65]:

$$\lambda^2 \frac{\partial^2 V}{\partial x^2} = \tau \frac{\partial V}{\partial t} + V$$

Once the intermediate unit V_2 is excited above a threshold voltage V_t, the unit is activated and self-excited up to a voltage V_a. This process then repeats *ad infinitum* along the entirety of the axon (assuming no backflow of the charge). The conduction velocity (i.e., the rate of this voltage flow) is thus inversely proportional to the reset time t_{reset} (the first time when $V_2(t) = V_t$ and $V_2(0) = V_{rest}$). Over the discrete lattice described above, the cable equation is given by:

$$\lambda^2 \frac{V_3 - 2V_2 + V_1}{h^2} - \tau \frac{dV_2}{dt} = V_2$$

Solving this for $V_2(t)$ and substituting in the boundary conditions, we find:

$$V_2(t) = \frac{\lambda^2 (V_{rest} + V_a)}{h^2 + 2\lambda^2} + K e^{\frac{-1}{\tau}\left(1 + \frac{2\lambda^2}{h^2}\right)t} = V_B + K e^{\frac{-1}{\tau}\left(1 + \frac{2\lambda^2}{h^2}\right)t}$$

where K is an integration constant needed to satisfy the initial condition $V_2(0) = V_{rest}$. Substituting in the initial condition and solving for t_{reset}, we find:

$$t_{reset} = \frac{-\tau}{1 + \frac{2\lambda^2}{h^2}} log \frac{V_t - V_B}{V_{rest} - V_B}$$

Thus:

$$CV \propto \frac{1}{log \frac{V_{rest} - V_B}{V_t - V_B}}$$

However, h is an arbitrarily small spacing that can approach zero. Thus:

$$CV \propto \frac{1}{log \frac{V_{rest} - V_a}{2V_t - V_{rest} - V_a}}$$

6.9 *Power and sample size calculations.*

The sample sizes for all statistical comparisons in this work were determined based on the means and pooled standard deviations from preliminary recordings of 8-10 cells or slices per group, α = 0.05, β = 0.8, corrected for the number of pairwise comparisons (τ), based on the following equations:

$$n = 2\left(\sigma \frac{z_{1-\alpha/(2\tau)} z_{1-\beta}}{\mu A - \mu B}\right)^2,$$

$$1 - \beta = \phi\left(z - z_{1-\alpha/(2\tau)}\right) + \phi\left(-z - z_{1-\alpha/(2\tau)}\right),$$

$$z = \frac{\mu A - \mu B}{\sigma\sqrt{\frac{2}{n}}},$$

where n is the sample size, σ is the standard deviation, ϕ is the standard normal distribution function, α is the Type I error rate, τ is the number of pairwise comparisons, and β is the Type II error rate. During the calculations, the normality of the residuals and equality of the variances were assumed *a priori*.

All of the calculations were performed with an online calculator available at:

http://powerandsamplesize.com/Calculators/Compare-k-Means/1-Way-ANOVA-Pairwise

7. **Acknowledgments**

We thank Dr. Vittorio Gallo (Children's National Research Institute, USA) for sharing his electrophysiology setup, without which this work would not have been possible; Dr. Kieran Clarke (University of Oxford) for providing D-βHb ester and advice; Dr. Joseph Abbah (Children's National Research Institute, USA) for help during the preliminary stage of the research; Dr. Richard L. Veech and Dr. M. Todd King (Lab of Metabolic Control, NIH/NIAAA, USA) for providing D-βHb ester and advice; Dr. Ting-Jiun Chen (Mt. Sinai Medical Center, USA) for help and advice with setting up the patch-clamp recordings; Dr. Peter Jonas (Institute of Science and Technology Austria, Austria) for providing the FBrain software; Dr Fernando Fernandez (Boston University, USA) for comments on the first draft of the manuscript; Dr Paul Hruz (Washington University School of Medicine in St. Louis, USA) for help with establishing the GluT4 inhibition model; Dr Nandkishore Prakash and Dave Saxon (Children's National Research Institute, USA) for advice and discussions; Dr Heidi Matos Galicia (National Institute of Neurological Disorders and Stroke, USA) for advice; Dr. Paul Cumming (Bern University Hospital) for critical reading of the manuscript; and members of the Mujica-Parodi laboratory (LCNeuro, USA) for discussions; C.W. also acknowledges support from the Marie-Josée Kravis Fellowship in Quantitative Biology.

8. **Funding**

This work was supported by the National Institutes of Health Grant K01NS110981 to N.A.S., the National Science Foundation NSF1926781 to L.M.P. and N.A.S., and the Department of Defense ARO W91NF2010189 to N.A.S.

9. **Contributions**

Conceptualization: BK, BA, CW, LMP, NAS

Methodology: BK, BA, FG, AB, JMH, CW, MK, LMP, NAS

Software: FG, AB, JMH, BA, CW, MK

Validation: BK, BA, CW, LMP, NAS

Formal Analysis: BK, BA, CW, FG, AB, JMH

Investigation: BK, BA, CW, FG, AB, JMH, LMP, NAS

715 **Writing – Original Draft**: BK

716 **Writing – Review & Editing**: BK, BA, CW, FG, AB, VV, JMH, MK, LMP, NAS

717 **Visualization**: BK, BA

718 **Supervision**: LMP, NAS

719 **Funding Acquisition**: LMP, NAS

720

721 10. **Conflicts of interest**

722 The authors declare no conflicts of interest.

723

724 11. **Data and materials availability**

725 The raw data presented in this work, data tables with analyses and tables with statistics are
726 available upon request. All code is available on GitHub by following the links provided in the text.

727

728 12. **References**

729 1. de la Monte SM. Insulin Resistance and Neurodegeneration: Progress Towards the
730 Development of New Therapeutics for Alzheimer's Disease. Drugs. 2017;77(1):47-65.
731 doi:10.1007/s40265-016-0674-0

732 2. De Felice FG, Ferreira ST. Inflammation, defective insulin signaling, and mitochondrial
733 dysfunction as common molecular denominators connecting type 2 diabetes to Alzheimer
734 disease. Diabetes. 2014;63(7):2262-2272. doi:10.2337/db13-1954

735 3. McNay EC, Recknagel AK. Brain insulin signaling: a key component of cognitive
736 processes and a potential basis for cognitive impairment in type 2 diabetes. Neurobiol Learn Mem.
737 2011;96(3):432-442. doi:10.1016/j.nlm.2011.08.005

738 4. Zhao WQ, Chen H, Quon MJ, Alkon DL. Insulin and the insulin receptor in experimental
739 models of learning and memory. Eur J Pharmacol. 2004;490(1-3):71-81.
740 doi:10.1016/j.ejphar.2004.02.045

741 5. McNay EC, Recknagel AK. Brain insulin signaling: a key component of cognitive
742 processes and a potential basis for cognitive impairment in type 2 diabetes. Neurobiol Learn Mem.

743 2011;96(3):432-442. doi:10.1016/j.nlm.2011.08.005

744 6. Ghasemi R, Haeri A, Dargahi L, Mohamed Z, Ahmadiani A. Insulin in the brain: sources,
745 localization and functions. Mol Neurobiol. 2013;47(1):145-171. doi:10.1007/s12035-012-8339-9

746 7. Kuwabara T, Kagalwala MN, Onuma Y, et al. Insulin biosynthesis in neuronal progenitors
747 derived from adult hippocampus and the olfactory bulb. EMBO Mol Med. 2011;3(12):742-754.
748 doi:10.1002/emmm.201100177

749 8. McNay EC, Pearson-Leary J. GluT4: A central player in hippocampal memory and brain
750 insulin resistance. Exp Neurol. 2020;323:113076. doi:10.1016/j.expneurol.2019.113076

751 9. Craft S. Insulin resistance syndrome and Alzheimer's disease: age- and obesity-related
752 effects on memory, amyloid, and inflammation. Neurobiol Aging. 2005;26 Suppl 1:65-69.
753 doi:10.1016/j.neurobiolaging.2005.08.021

754 10. Kerti L, Witte AV, Winkler A, Grittner U, Rujescu D, Flöel A. Higher glucose levels
755 associated with lower memory and reduced hippocampal microstructure. Neurology.
756 2013;81(20):1746-1752. doi:10.1212/01.wnl.0000435561.00234.ee

757 11. Antal B, McMahon LP, Sultan SF, et al. Type 2 diabetes mellitus accelerates brain aging
758 and cognitive decline: Complementary findings from UK Biobank and meta-analyses. Elife.
759 2022;11:e73138. Published 2022 May 24. doi:10.7554/eLife.73138

760 12. McEwen BS, Reagan LP. Glucose transporter expression in the central nervous system:
761 relationship to synaptic function. Eur J Pharmacol. 2004;490(1-3):13-24.
762 doi:10.1016/j.ejphar.2004.02.041

763 13. Pearson-Leary J, McNay EC. Novel Roles for the Insulin-Regulated Glucose Transporter-
764 4 in Hippocampally Dependent Memory. J Neurosci. 2016;36(47):11851-11864.
765 doi:10.1523/JNEUROSCI.1700-16.2016

766 14. McNay EC, Fries TM, Gold PE. Decreases in rat extracellular hippocampal glucose
767 concentration associated with cognitive demand during a spatial task. Proc Natl Acad Sci U S A.
768 2000;97(6):2881-2885. doi:10.1073/pnas.0583697

769 15. Grillo CA, Piroli GG, Hendry RM, Reagan LP. Insulin-stimulated translocation of GLUT4
770 to the plasma membrane in rat hippocampus is PI3-kinase dependent. Brain Res. 2009;1296:35-
771 45. doi:10.1016/j.brainres.2009.08.005

772 16. Stranahan AM, Norman ED, Lee K, et al. Diet-induced insulin resistance impairs
773 hippocampal synaptic plasticity and cognition in middle-aged rats. Hippocampus.
774 2008;18(11):1085-1088. doi:10.1002/hipo.20470

775 17. Ashrafi G, Wu Z, Farrell RJ, Ryan TA. GLUT4 Mobilization Supports Energetic Demands
776 of Active Synapses. Neuron. 2017;93(3):606-615.e3. doi:10.1016/j.neuron.2016.12.020

777 18. De Felice FG, Ferreira ST. Inflammation, defective insulin signaling, and mitochondrial
778 dysfunction as common molecular denominators connecting type 2 diabetes to Alzheimer
779 disease. Diabetes. 2014;63(7):2262-2272. doi:10.2337/db13-1954

780 19. Kothari V, Luo Y, Tornabene T, et al. High fat diet induces brain insulin resistance and
781 cognitive impairment in mice. Biochim Biophys Acta Mol Basis Dis. 2017;1863(2):499-8.
782 doi:10.1016/j.bbadis.2016.10.006

783 20. Martínez-François JR, Fernández-Agüera MC, Nathwani N, et al. BAD and KATP
784 channels regulate neuron excitability and epileptiform activity. Elife. 2018;7:e32721. Published
785 2018 Jan 25. doi:10.7554/eLife.32721

786 21. Kashiwaya Y, Takeshima T, Mori N, Nakashima K, Clarke K, Veech RL. D-beta-
787 hydroxybutyrate protects neurons in models of Alzheimer's and Parkinson's disease. Proc Natl
788 Acad Sci U S A. 2000;97(10):5440-5444. doi:10.1073/pnas.97.10.5440

789 22. Chikahisa S, Shimizu N, Shiuchi T, Séi H. Ketone body metabolism and sleep
790 homeostasis in mice. Neuropharmacology. 2014;79:399-404.
791 doi:10.1016/j.neuropharm.2013.12.009

792 23. Puchalska P, Crawford PA. Multi-dimensional Roles of Ketone Bodies in Fuel Metabolism,
793 Signaling, and Therapeutics. Cell Metab. 2017;25(2):262-284. doi:10.1016/j.cmet.2016.12.022

794 24. Ma W, Berg J, Yellen G. Ketogenic diet metabolites reduce firing in central neurons by
795 opening K(ATP) channels. J Neurosci. 2007;27(14):3618-3625. doi:10.1523/JNEUROSCI.0132-
796 07.2007

797 25. Jensen NJ, Wodschow HZ, Nilsson M, Rungby J. Effects of Ketone Bodies on Brain
798 Metabolism and Function in Neurodegenerative Diseases. Int J Mol Sci. 2020;21(22):8767.
799 Published 2020 Nov 20. doi:10.3390/ijms21228767

800 26. Hartman AL, Gasior M, Vining EP, Rogawski MA. The neuropharmacology of the
801 ketogenic diet. Pediatr Neurol. 2007;36(5):281-292. doi:10.1016/j.pediatrneurol.2007.02.008

802 27. Xin L, Ipek Ö, Beaumont M, et al. Nutritional Ketosis Increases NAD+/NADH Ratio in
803 Healthy Human Brain: An in Vivo Study by 31P-MRS. Front Nutr. 2018;5:62. Published 2018 Jul
804 12. doi:10.3389/fnut.2018.00062

805 28. Maalouf M, Sullivan PG, Davis L, Kim DY, Rho JM. Ketones inhibit mitochondrial
806 production of reactive oxygen species production following glutamate excitotoxicity by increasing

807 NADH oxidation. Neuroscience. 2007;145(1):256-264. doi:10.1016/j.neuroscience.2006.11.06

808 29. Shimazu T, Hirschey MD, Newman J, et al. Suppression of oxidative stress by β-
809 hydroxybutyrate, an endogenous histone deacetylase inhibitor. Science. 2013;339(6116):211-
810 214. doi:10.1126/science.1227166

811 30. Lutas A, Yellen G. The ketogenic diet: metabolic influences on brain excitability and
812 epilepsy. Trends Neurosci. 2013;36(1):32-40. doi:10.1016/j.tins.2012.11.005

813 31. Clarke K, Tchabanenko K, Pawlosky R, et al. Kinetics, safety and tolerability of (R)-3-
814 hydroxybutyl (R)-3-hydroxybutyrate in healthy adult subjects. Regul Toxicol Pharmacol.
815 2012;63(3):401-408. doi:10.1016/j.yrtph.2012.04.008

816 32. Kesl SL, Poff AM, Ward NP, et al. Effects of exogenous ketone supplementation on blood
817 ketone, glucose, triglyceride, and lipoprotein levels in Sprague-Dawley rats. Nutr Metab (Lond).
818 2016;13:9. Published 2016 Feb 4. doi:10.1186/s12986-016-0069-y

819 33. Weistuch C, Mujica-Parodi LR, Razban RM, et al. Metabolism modulates network
820 synchrony in the aging brain. Proc Natl Acad Sci U S A. 2021;118(40):e2025727118.
821 doi:10.1073/pnas.2025727118

822 34. Mujica-Parodi LR, Amgalan A, Sultan SF, et al. Diet modulates brain network stability, a
823 biomarker for brain aging, in young adults. Proc Natl Acad Sci U S A. 2020;117(11):6170-6177.
824 doi:10.1073/pnas.1913042117

825 35. Hruz PW, Murata H, Qiu H, Mueckler M. Indinavir induces acute and reversible peripheral
826 insulin resistance in rats. Diabetes. 2002;51(4):937-942. doi:10.2337/diabetes.51.4.937

827 36. Hresko RC, Hruz PW. HIV protease inhibitors act as competitive inhibitors of the
828 cytoplasmic glucose binding site of GLUTs with differing affinities for GLUT1 and GLUT4. PLoS
829 One. 2011;6(9):e25237. doi:10.1371/journal.pone.0025237

830 37. Colgin LL, Denninger T, Fyhn M, et al. Frequency of gamma oscillations routes flow of
831 information in the hippocampus. Nature. 2009;462(7271):353-357. doi:10.1038/nature08573

832 38. Buzsáki G, Wang XJ. Mechanisms of gamma oscillations. Annu Rev Neurosci.
833 2012;35:203-225. doi:10.1146/annurev-neuro-062111-1444

834 39. Catterall WA. From ionic currents to molecular mechanisms: the structure and function of
835 voltage-gated sodium channels. Neuron. 2000;26(1):13-25. doi:10.1016/s0896-6273(00)81133-2

836 40. Howarth C, Gleeson P, Attwell D. Updated energy budgets for neural computation in the
837 neocortex and cerebellum. J Cereb Blood Flow Metab. 2012;32(7):1222-1232.

838 doi:10.1038/jcbfm.2012.35

839 41. Lujan B, Kushmerick C, Banerjee TD, Dagda RK, Renden R. Glycolysis selectively shapes
840 the presynaptic action potential waveform. J Neurophysiol. 2016;116(6):2523-2540.
841 doi:10.1152/jn.00629.2016

842 42. Padamsey Z, Katsanevaki D, Dupuy N, Rochefort NL. Neocortex saves energy by
843 reducing coding precision during food scarcity. Neuron. 2022;110(2):280-296.e10.
844 doi:10.1016/j.neuron.2021.10.024

845 43. Jensen TP, Zheng K, Cole N, Marvin JS, Looger LL, Rusakov DA. Multiplex imaging
846 relates quantal glutamate release to presynaptic Ca2+ homeostasis at multiple synapses in situ.
847 Nat Commun. 2019;10(1):1414. Published 2019 Mar 29. doi:10.1038/s41467-019-09216-8

848 44. Newman JC, Verdin E. β-Hydroxybutyrate: A Signaling Metabolite. Annu Rev Nutr.
849 2017;37:51-76. doi:10.1146/annurev-nutr-071816-064916

850 45. Lund TM, Obel LF, Risa Ø, Sonnewald U. β-Hydroxybutyrate is the preferred substrate for
851 GABA and glutamate synthesis while glucose is indispensable during depolarization in cultured
852 GABAergic neurons. Neurochem Int. 2011;59(2):309-318. doi:10.1016/j.neuint.2011.06.002

853 46. Scott RS, Henneberger C, Padmashri R, Anders S, Jensen TP, Rusakov DA. Neuronal
854 adaptation involves rapid expansion of the action potential initiation site. *Nat Commun*.
855 2014;5:3817. Published 2014 May 23. doi:10.1038/ncomms4817

856 47. Stranahan AM, Mattson MP. Impact of energy intake and expenditure on neuronal
857 plasticity. Neuromolecular Med. 2008;10(4):209-218. doi:10.1007/s12017-008-8043-0

858 48. Piroli GG, Grillo CA, Reznikov LR, et al. Corticosterone impairs insulin-stimulated
859 translocation of GLUT4 in the rat hippocampus. Neuroendocrinology. 2007;85(2):71-80.
860 doi:10.1159/000101694

861 49. Grillo CA, Piroli GG, Hendry RM, Reagan LP. Insulin-stimulated translocation of GLUT4
862 to the plasma membrane in rat hippocampus is PI3-kinase dependent. Brain Res. 2009;1296:35-
863 45. doi:10.1016/j.brainres.2009.08.005

864 50. Leloup C, Arluison M, Kassis N, et al. Discrete brain areas express the insulin-responsive
865 glucose transporter GLUT4. Brain Res Mol Brain Res. 1996;38(1):45-53. doi:10.1016/0169-
866 328x(95)00306-d

867 51. Vannucci SJ, Koehler-Stec EM, Li K, Reynolds TH, Clark R, Simpson IA. GLUT4 glucose
868 transporter expression in rodent brain: effect of diabetes. Brain Res. 1998;797(1):1-11.
869 doi:10.1016/s0006-8993(98)00103-6

52. 42. Miranda M, Morici JF, Zanoni MB, Bekinschtein P. Brain-Derived Neurotrophic Factor: A Key Molecule for Memory in the Healthy and the Pathological Brain. Front Cell Neurosci. 2019;13:363. Published 2019 Aug 7. doi:10.3389/fncel.2019.00363

53. Won SJ, Yoo BH, Kauppinen TM, et al. Recurrent/moderate hypoglycemia induces hippocampal dendritic injury, microglial activation, and cognitive impairment in diabetic rats. J Neuroinflammation. 2012;9:182. Published 2012 Jul 25. doi:10.1186/1742-2094-9-182

54. 44. Yamada KA, Rensing N, Izumi Y, et al. Repetitive hypoglycemia in young rats impairs hippocampal long-term potentiation. Pediatr Res. 2004;55(3):372-379. doi:10.1203/01.PDR.0000110523.07240.C

55. Lee SY, Kim JH. Mechanisms underlying presynaptic Ca2+ transient and vesicular glutamate release at a CNS nerve terminal during in vitro ischaemia. J Physiol. 2015;593(13):2793-2806. doi:10.1113/JP270060

56. García-Rodríguez D, Giménez-Cassina A. Ketone Bodies in the Brain Beyond Fuel Metabolism: From Excitability to Gene Expression and Cell Signaling. Front Mol Neurosci. 2021;14:732120. Published 2021 Aug 27. doi:10.3389/fnmol.2021.732120

57. van Nieuwenhuizen, H., Chesebro, A. G., Polizu, C., Clarke, K., Strey, H. H., Weistuch, C., & Mujica-Parodi, L. R. Ketosis regulates K+ ion channels, strengthening brain-wide signaling disrupted by age. *bioRxiv*, 2023-05.

58. Ma W, Berg J, Yellen G. Ketogenic diet metabolites reduce firing in central neurons by opening K(ATP) channels. J Neurosci. 2007;27(14):3618-3625. doi:10.1523/JNEUROSCI.0132-07.2007

59. Tanner GR, Lutas A, Martínez-François JR, Yellen G. Single K ATP channel opening in response to action potential firing in mouse dentate granule neurons. J Neurosci. 2011;31(23):8689-8696. doi:10.1523/JNEUROSCI.5951-10.2011

60. Martínez-François JR, Fernández-Agüera MC, Nathwani N, et al. BAD and KATP channels regulate neuron excitability and epileptiform activity. Elife. 2018;7:e32721. Published 2018 Jan 25. doi:10.7554/eLife.32721

61. Lund TM, Ploug KB, Iversen A, Jensen AA, Jansen-Olesen I. The metabolic impact of β-hydroxybutyrate on neurotransmission: Reduced glycolysis mediates changes in calcium responses and KATP channel receptor sensitivity. J Neurochem. 2015;132(5):520-531. doi:10.1111/jnc.12975

62. Fremeau RT Jr, Kam K, Qureshi T, et al. Vesicular glutamate transporters 1 and 2 target to functionally distinct synaptic release sites. Science. 2004;304(5678):1815-1819.

904 doi:10.1126/science.1097468

905 63. Juge N, Gray JA, Omote H, et al. Metabolic control of vesicular glutamate transport and
906 release. Neuron. 2010;68(1):99-112. doi:10.1016/j.neuron.2010.09.002

907 64. Pernía-Andrade AJ, Goswami SP, Stickler Y, Fröbe U, Schlögl A, Jonas P. A
908 deconvolution-based method with high sensitivity and temporal resolution for detection of
909 spontaneous synaptic currents in vitro and in vivo. Biophys J. 2012;103(7):1429-1439.
910 doi:10.1016/j.bpj.2012.08.039

911 65. Koch C, Chapter 6: The Hodgkin and Huxley Model of Action Potential Generation. In:
912 Koch C, Biophysics of Computation: Information Processing in Single Neurons. Oxford University
913 Press. 2004. p. 139-176. Print.

914 66. Traub RD, Wong RK, Miles R, Michelson H. A model of a CA3 hippocampal pyramidal
915 neuron incorporating voltage-clamp data on intrinsic conductances. J Neurophysiol.
916 1991;66(2):635-6. doi:10.1152/jn.1991.66.2.635

917 67. Yu N, Morris CE, Joós B, Longtin A. Spontaneous excitation patterns computed for axons
918 with injury-like impairments of sodium channels and Na/K pumps. PLoS Comput Biol.
919 2012;8(9):e1002664. doi:10.1371/journal.pcbi.1002664

920 68. Altemus KL, Lavenex P, Ishizuka N, Amaral DG. Morphological characteristics and
921 electrophysiological properties of CA1 pyramidal neurons in macaque monkeys. Neuroscience.
922 2005;136(3):741-756. doi:10.1016/j.neuroscience.2005.07.001

923

924 13. **Figures.**

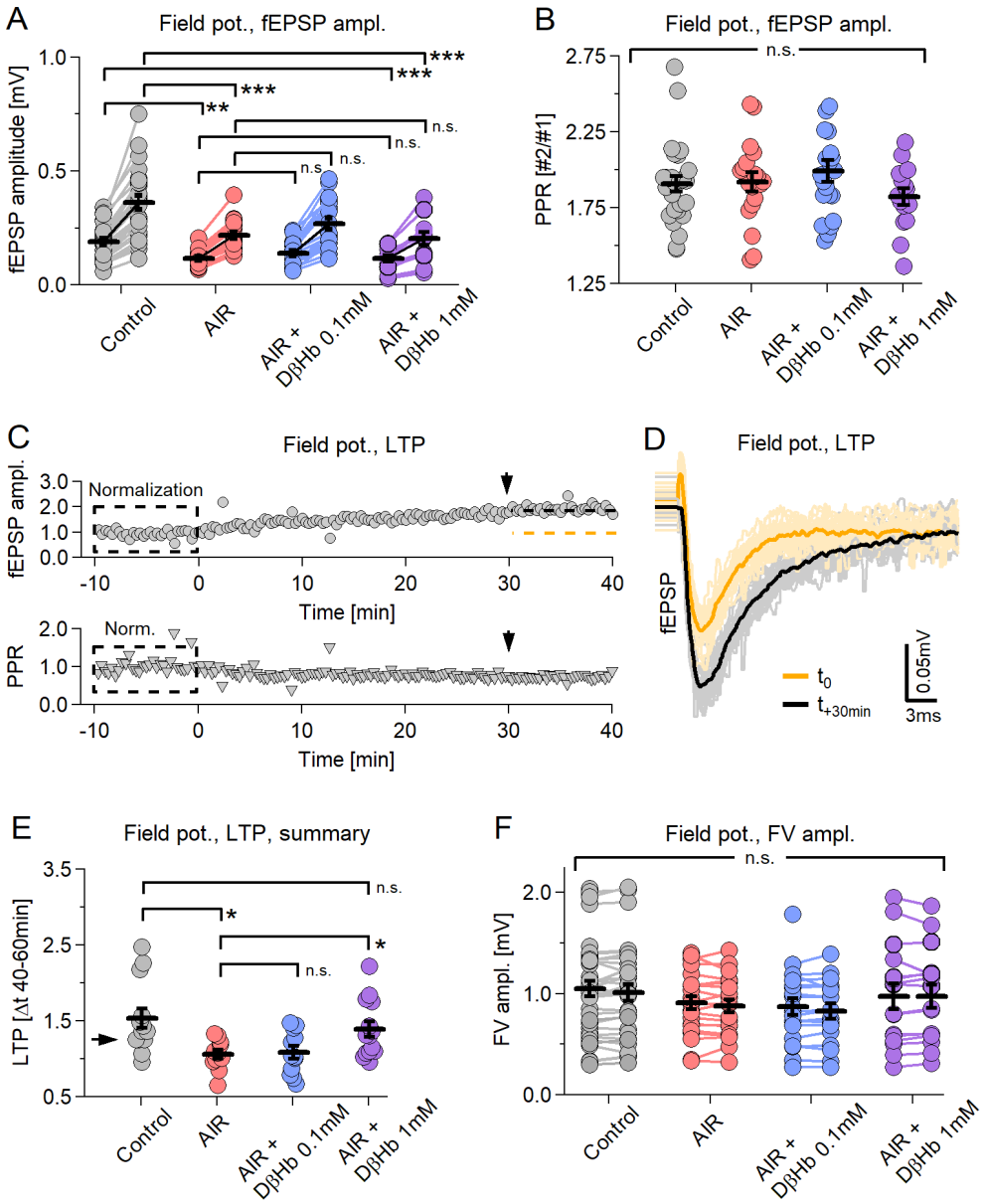

Figure 1: Synaptic activity and LTP, but not neuronal firing or PPR, decrease during paired stimulation under AIR conditions and do not recover during D-βHb administration.

A) Scatter plot of the fEPSP amplitudes evoked by paired-pulse stimulation of Schaffer collaterals. Each pair of circles is the average of 30-40 consecutive responses. The black bars represent the mean ± SEM. Control fEPSPs in gray, AIR in red; 0.1 mM D-βHb+AIR in blue; 1 mM D-βHb+AIR in purple. Control: n=26 slices; AIR n=19; 0.1 mM D-βHb+AIR: n=20; 1 mM D-βHb+AIR: n=16. B) Scatter plot of the paired-pulse ratio (PPR) of the fEPSPs recorded in A. The labels, n, are identical to those in A). There were no significant differences (p=0.41, ANOVA). C) On top: Representative recording of a control experiment in which paired stimulation was applied for 50

934 min. Each circle represents the fEPSP amplitude normalized to the average of the first 30 fEPSPs.
935 The dashed orange line represents the mean amplitude at time -10 to 0 min. The black line
936 represents the mean amplitude at +30 to +40 min. Bottom: corresponding normalized PPR. D)
937 fEPSP waveforms recorded in C), showing LTP development. In gray, 30 fEPSP waveforms at
938 t=0 ± 5 min and their average (black). In yellow, 30 fEPSP waveforms at t=+30 ± 5 min and their
939 average (orange). Stimulation artifacts and FVs are removed. E) Scatter plot of LTP signals
940 triggered by paired stimulation. Control: n=13; AIR n=11; 0.1 mM D-βHb+AIR: n=12; 1 mM D-
941 βHb+AIR: n=14. F) Scatter plot of the FV amplitudes recorded during A). The labels, n, are
942 identical to those in A). There were no significant differences (p=0.42, p=0.40; ANOVA). In all
943 plots, *p<0.05; **p<0.01; ***p<0.001.

944

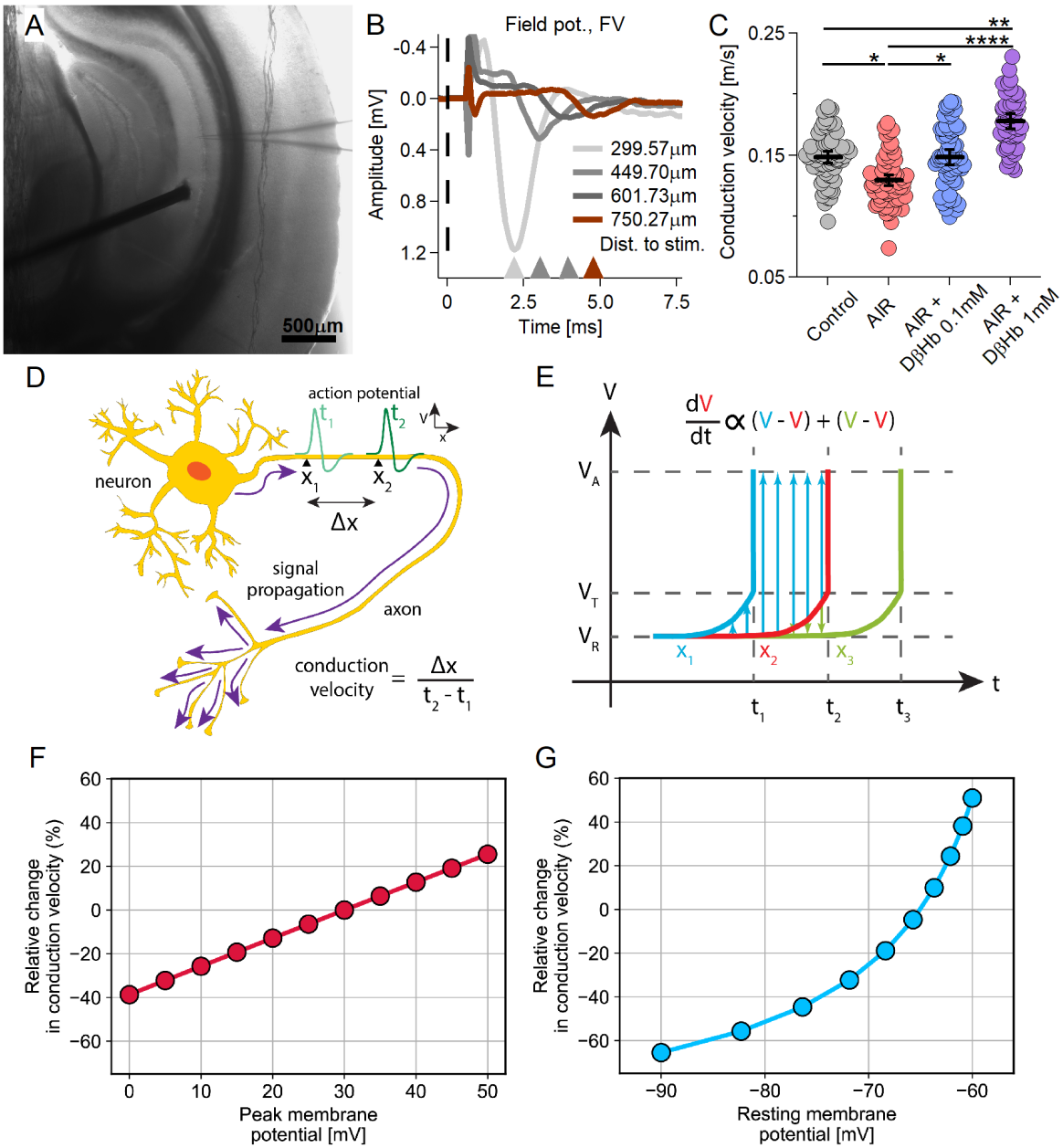

Figure 2: Conduction velocity (CV) of Schaffer collaterals decreases under AIR conditions, is rescued by 0.1 mM D-βHb, and increases with 1 mM D-βHb.

A) Representative hippocampal slice during CV recording. B) Representative averaged FV waveforms recorded in CA1. The stimulus onset time (t=0) is marked with a dashed line. Stimulus artifacts are removed. C) CV scatter plots. Each colored circle represents a CV replicate. Control in gray, AIR in light red, 0.1 mM D-βHb+AIR in blue, and 1 mM D-βHb+AIR in purple. Data are shown as the mean ± SEM. *p<0.05; ***p<0.001, nested ANOVA, Control: m=62, n=24, N=14;

AIR: m=65, n=22, N=13; 0.1 mM D-βHb+AIR: m=64, n=21, N=13; 1 mM D-βHb+AIR: m=50, n=14, N=10. D) Diagram of the CV of an AP propagating along an axon: distance along the axon (Δx) and the time needed for an AP to pass that distance (t_2-t_1). V represents the membrane potential. E) Model of a propagating AP. The change in V(t) is shown at longitudinal increments along the axon (x_2) and at neighboring increments immediately before (x_1) and behind (x_3). The membrane potential at rest (VR) changes over time proportionally to the sum of differences between its value and those of the preceding and superseding increments. Upon reaching the threshold potential (VT), a spike occurs, and the membrane potential reaches the peak value (VA). F-G) CV is modulated by VA and VR. Our computational model predicts declining CV due to reductions in the peak AP (F) and/or hyperpolarization of the resting membrane potential (G). The CV is quantified as a percentage relative to the control.

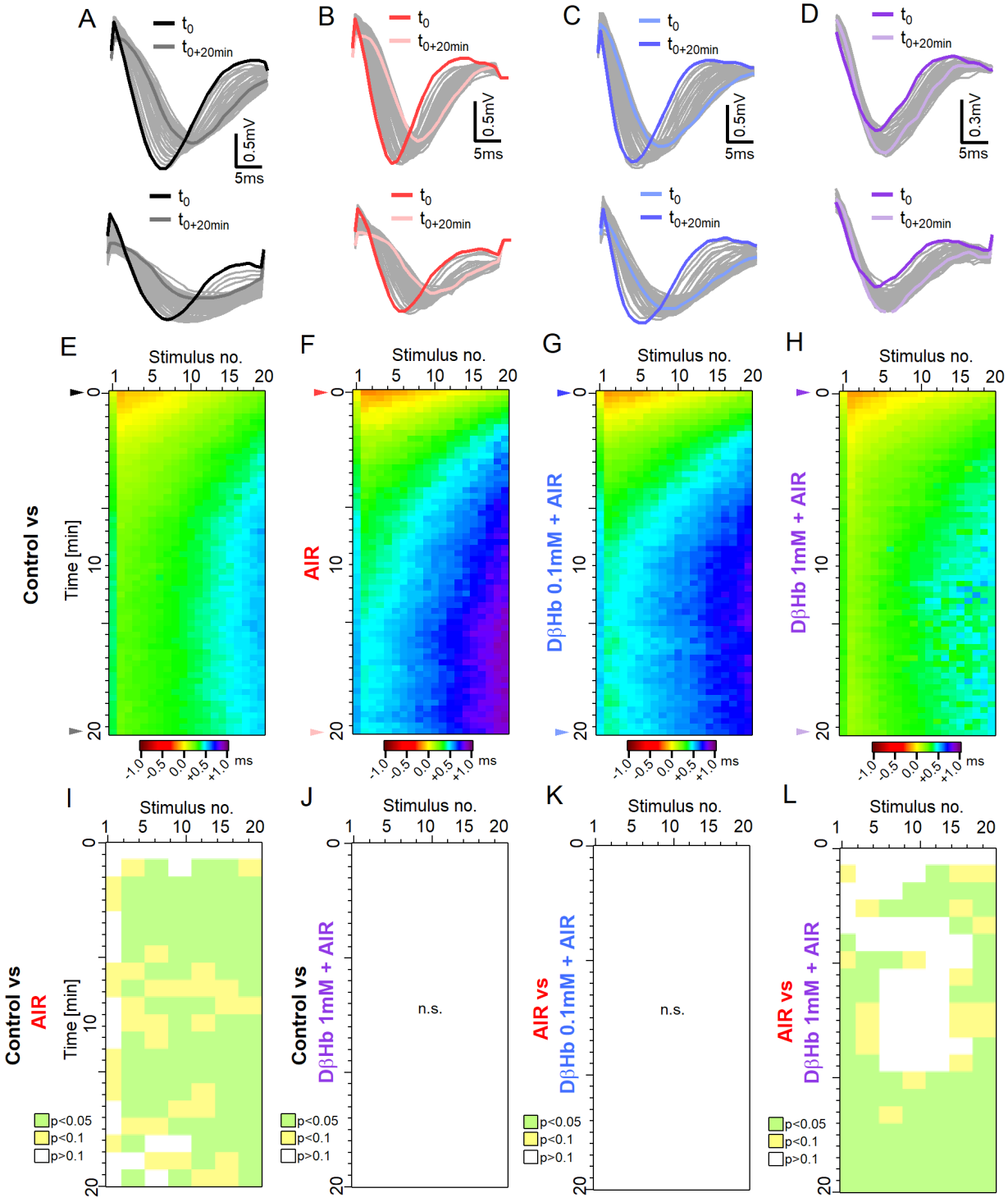

964 **Figure 3**: Time delays in axonal firing during train stimulation are increased during AIR and
965 reversed by 1 mM D-βHb.

A) Top: Representative example of the FVs recorded at the first stimulus in the control group during stimulation with 20 pulses applied at 25 Hz every 20 s over 20 min. Bottom: FVs recorded in response to the last stimulus in each train. The FVs recorded at t=0 are marked in black; the FVs recorded at t=+20 min are marked in dark gray. B) - D) The same as A) in the AIR, 0.1 mM D-βHb+AIR and 1 mM D-βHb+AIR groups. E) Heatmap of the mean, normalized FV peak latencies recorded in the Control group. Each trial is represented by a new row. The columns represent the time points of successive stimuli. Normalized latencies (0 ms) are color-coded in yellow. Delays (>0 ms) are color-coded in green–violet, and latency improvements (<0 ms) are color-coded in orange–brown. n=24, N=22. F) - H) The same as E) for AIR, n=16, N=15; 0.1 mM D-βHb+AIR. n=17, N=15, 1 mM D-βHb+AIR. n=14, N=10. I) Statistical comparison of latencies for the Control (E) and AIR (F) groups, performed based on means of 3 stimuli x 2 trials blocks. p<0.05 in green, p<0.1 in yellow, p≥0.1 in white. J) The same as I) comparing the results of the Control (E) and 1 mM D-βHb+AIR (H) groups. There were no significant differences, p=0.067 to p=0.99. K) The same as I) comparing the results of the AIR (F) and 0.1 mM D-βHb+AIR (G) groups. There were no significant differences, p=0.41 to p=0.99. L) The same as I) comparing the results of the AIR (F) and 1 mM D-βHb+AIR (H) groups.

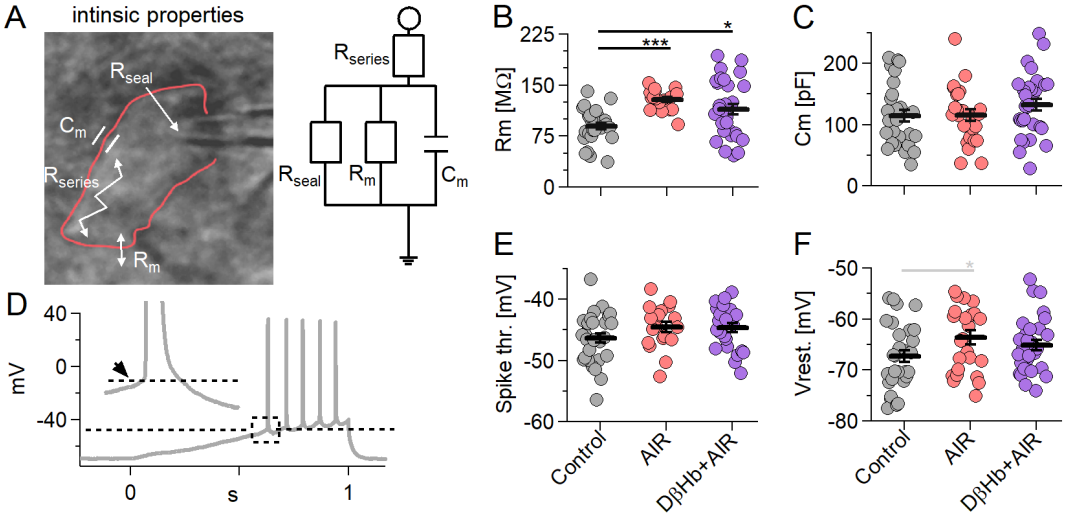

Figure 4: Membrane resistance (R_m) increases during AIR and is not reversed by D-βHb. Other intrinsic properties did not change under either condition.

A) Left: A CA1 pyramidal neuron recorded in whole-cell patch-clamp mode (outlined in red), with resistances and capacitance denoted within the cell. Right: A simple electric circuit diagram of a cell with the same resistances. B) Scatter plots of CA1 pyramidal neuron Rm compared among the experimental groups. Each colored circle represents a value recorded in a single cell. Control in gray, AIR in light red, 1 mM D-βHb+AIR in purple. Vertical black bars represent the mean ± SEM. C) Scatter plots of CA1 pyramidal neurons Cm compared among the experimental groups. The plots and coloring are identical to B). There were no significant differences (p=0.32). D)

Representative example of a 300 pA ramp current injection performed in a control CA1 pyramidal neuron. The dashed line marks the onset (spike threshold) of the first AP. The inset shows the magnified appreciate, with the arrow pointing to the onset. E) Scatter plots of CA1 pyramidal neuron spike thresholds compared among the experimental groups. The plots are identical to B). There were no significant differences (p=0.17). F) Scatter plots of CA1 pyramidal neurons RMP (V_{rest}) compared among the experimental groups. The plots and coloring are identical to B). There were no significant differences (p=0.09). Control n=28, N=22; AIR n=25, N=17; 1 mM D-βHb+AIR; n=30, N=16. In black, *p<0.05; **p<0.01; ***p<0.001; in gray *p<0.1.3.3 AIR adversely affects input timing, which is restored by high D-βHb concentrations.

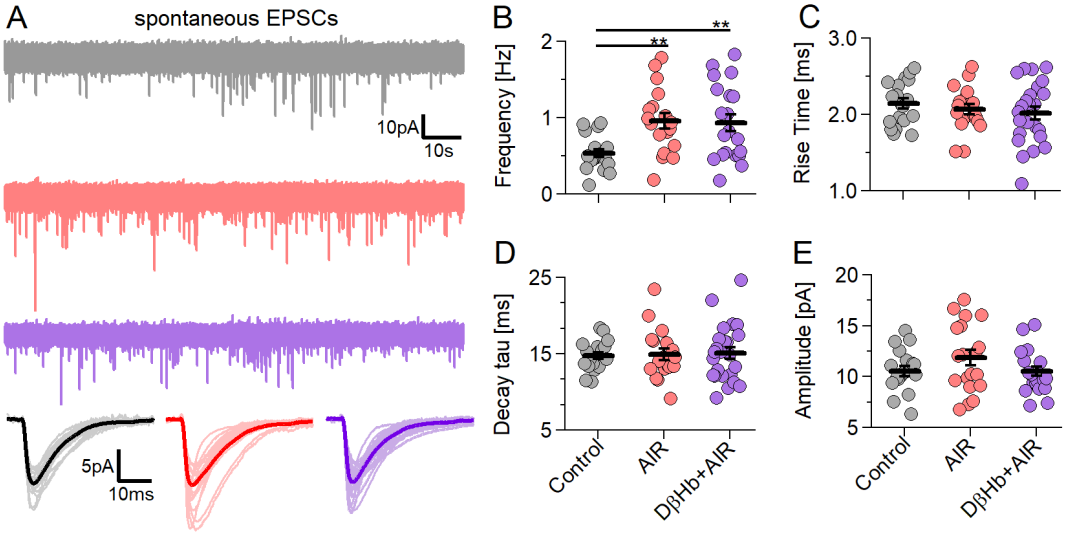

Figure 5: AIR increased sEPSC frequency without altering sEPSC properties, and D-βHb administration did not reverse this effect.

A) Representative examples of the first 2 min of sEPSC waveforms recorded in CA1 pyramidal neurons, voltage clamped at V_h= -70 mV (Control in gray; AIR in red; 1.0 mM D-βHb+AIR in purple). Bottom: averaged sEPSC waveforms from individual cells (light color) and the group mean (full color). B) Scatter plots of the sEPSC frequency recorded in CA1 pyramidal neurons compared among the experimental groups. Each colored circle represents the frequency recorded in a single cell. The labels are the same as in A). Vertical black bars represent the mean ± SEM. *p<0.05. C) Scatter plots of the sEPSC 20-80% rise times, labeled as in B). There were no significant differences (p=0.51). D) Scatter plots of the sEPSC decay tau times, labeled as in B). There were no significant differences (p=0.98). E) Scatter plots of the sEPSC amplitudes, labeled as in B). There were no significant differences (p=0.21). Control n=19, N=19; AIR n=19, N=14; 1 mM D-βHb+AIR, n=23, N=16. **p<0.01.

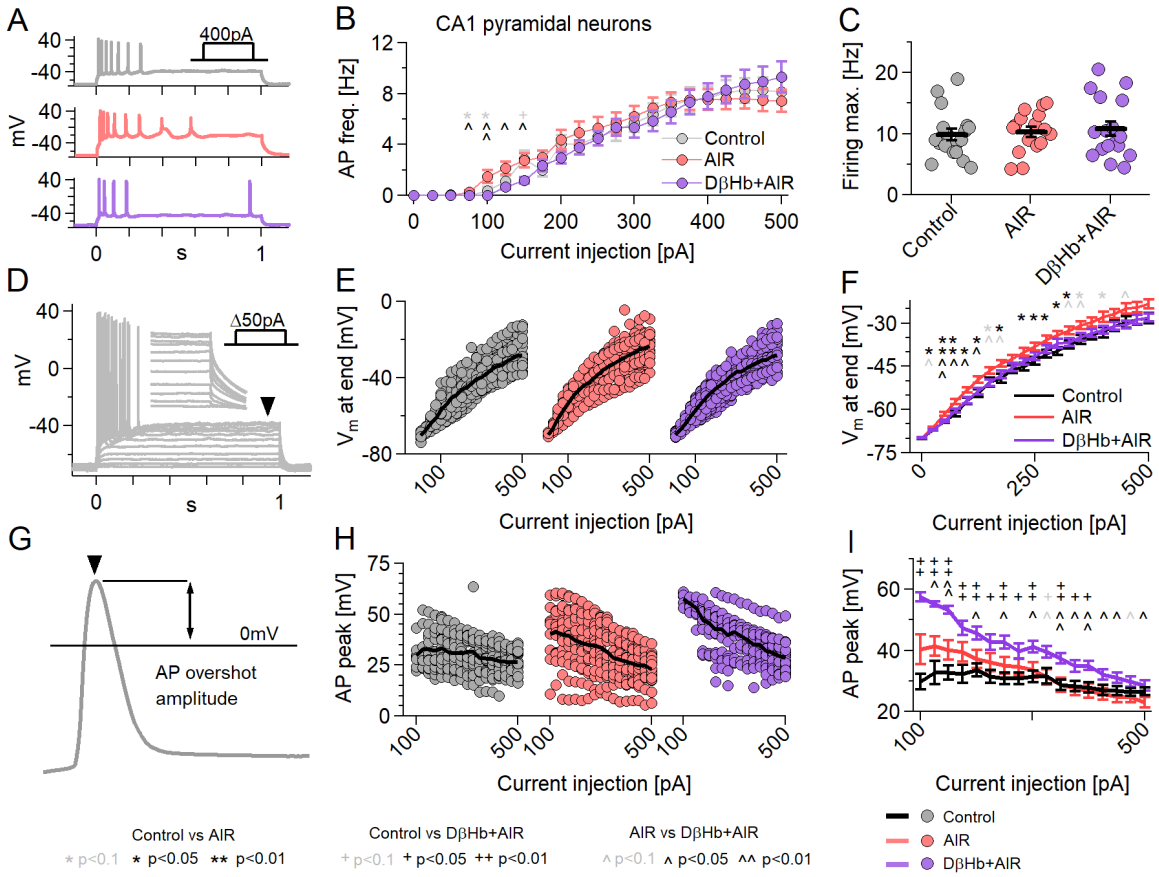

Figure 6: Neuronal firing is mildly affected by AIR and reversed by D-βHb, with D-βHb increasing AP overshoot amplitudes.

A) Representative examples of responses to 400 pA square current injections into control (gray), AIR (red), and 1 mM D-βHb+AIR (purple) CA1 pyramidal neurons, held at V_h=-70 mV. B) I-O curves of CA1 pyramidal neurons receiving 21, Δ+25 pA injections (max. 0 pA; V_h=-70 mV). Circles represent the group mean ± SEM. * Control vs. AIR, + Control vs. 1 mM D-βHb+AIR, ^ AIR vs. 1 mM D-βHb+AIR. *,+,^ in black p<0.05; **,++,^^ in black p<0.01; *,+,^ in gray p<0.1; ANOVA) Maximum firing rate of the pyramidal neurons in B). Circles represent single neurons; black bars represent group mean ± SEM. There were no significant differences (p=0.778, ANOVA). D) Example of responses to Δ+25 pA square current injections into a control pyramidal neuron. The arrowhead and inset mark the final membrane depolarization (V_m, last 5 ms of the step). E) Vm at the current injections from B). F) Group mean ± SEM of V_m from E). Statistical tests and labels are identical to B). Control n=23, N=20; AIR n=20, N=14; 1 mM D-βHb+AIR n=22, N=16. G) Example of AP overshoot measurement. The black line marks V_m= 0 mV. H) Averaged AP overshoot amplitudes from B). I) Group mean ± SEM of overshoot amplitudes from H).

Statistical tests and labels are identical to B). In all comparisons, Control n=23, N=20; AIR n=20, N=14; 1 mM D-βHb+AIR, n=22, N=16.

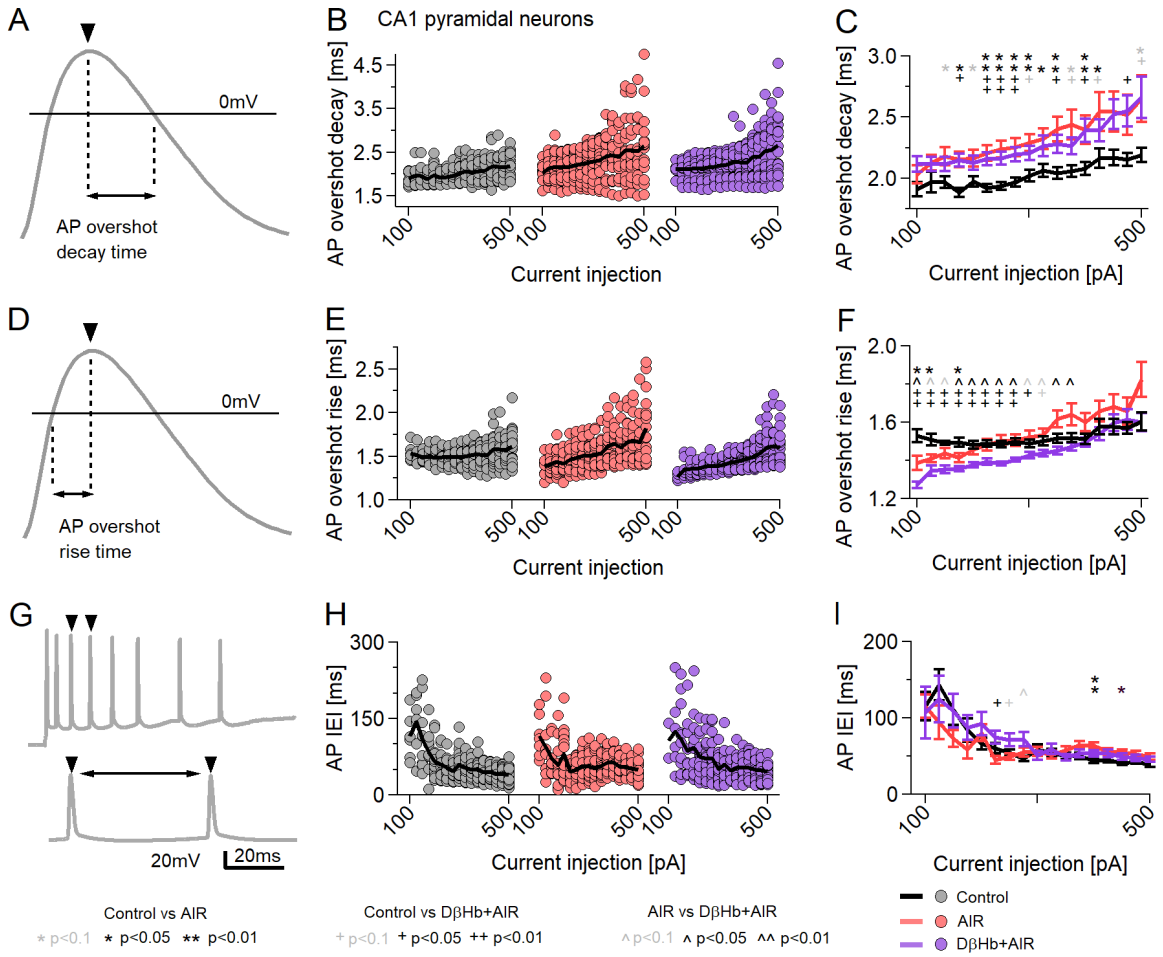

Figure 7: AP decay times change during AIR and D-βHb + AIR conditions, but D-βHb + AIR APs have faster rise times.

A) Example of AP decay time measurement. The black line marks V_m= 0 mV. B) Mean AP decay times for the current injections. Circles represent averaged amplitudes in single neurons. The black lines represent group means. C) Group mean ± SEM of AP decay times from B). Statistical tests and labels are identical to B). D) Example of AP decay time measurement. The black line marks V_m= 0 mV. E) Averaged AP rise times for the current injections in B). Circles represent averaged amplitudes in single neurons. The black lines represent group means. F) Group mean ± SEM of AP rise times from B). Statistical tests and labels are identical to B). G) An example of the AP IEI measurement. The double arrow marks the latency between AP peaks. H) Averaged IEI recorded during the injections in B). Each point represents the average IEI recorded at each step in a single neuron. The black line represents the group mean. I) Group mean ± SEM of

1046 averaged IEI. *,+,^ $p<0.05$; ANOVA. In all comparisons, Control n=23, N=20; AIR n=20, N=14; 1
1047 mM D-βHb+AIR, n=22, N=16.